TÉCNICO LISBOA

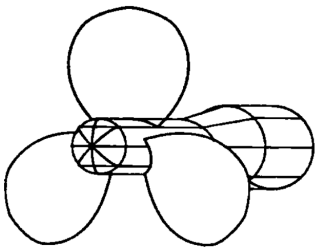

Analysis of the Flow in the Boundary Layer of a Marine Propeller Blade Calculated with a RANSE Method

Arnau Jovell Megias

Thesis to obtain the Master of Science Degree in

Aerospace Engineering

Supervisor: Dr. João Manuel Ribeiro Costa Baltazar

Examination Committee

Chairperson: Prof. Filipe Szolnoky Ramos Pinto Cunha

Supervisor: Dr. João Manuel Ribeiro Costa Baltazar

Member of the Committee: Prof. Luís Rego da Cunha de Eça

February 2021

Declaration

I declare that this document is an original work of my own authorship and that it fulfils all the requirements of the Code of Conduct and Good Practices of the Universidade de Lisboa.

Acknowledgments

I would like to thank Dr. João Baltazar for all the help and guidance he has provided during the development of this Master Thesis. I would also like to thank the MARIN for granting Dr. Baltazar and me access to their clusters to run the most computationally heavy simulations of the Thesis.

Finally, I would like to thank my family and friends who, as always, have accompanied me throughout this journey and have supported me along the way.

Resumo

Os modelos RANS têm sido e são utilizados nas áreas da Engenharia Naval e Aeronáutica em investigações de Mecânica de Fluídos Computacional pelo seu grande potencial para a previsão da *performance* de rotores. Tal é o seu potencial que ainda é uma área de investigação em áreas de engenharia. Nesta Tese, o objetivo principal é obter os resultados de parâmetros relevantes da camada limite num hélice marítimo a partir de cálculos RANSE. Dois modelos de turbulência são utilizados para a previsão da performance do hélice e para a comparação com os resultados experimentais obtidos por Jessup em 1984. Uma validação numérica dos resultados também é feita, onde a incerteza numérica e o erro de discretização são estimados.

Os resultados obtidos mostram uns valores de incerteza numérica a erro muito aceptáveis, e geralmente uma boa concordância dos resultados simulados com os dados experimentais. Ainda que os dois modelos apresentam resultados parecidos mas diferentes, o modelo $\gamma - \tilde{Re}_{\theta_t}$ é considerado ser mais adequado para este trabalho, já que inclui uma região de camada limite laminar e outra turbulenta, com a região de transição no meio. O modelo $k-\omega$ SST é considerado não tão bom neste caso tratado aqui.

Palavras-chave: Modelo de turbulência e transição, Hélice marítimo, RANSE, Simulação

Abstract

RANS models have been and are used in Marine and Aeronautical Engineering in CFD investigations for their big potential to predict, among other things, propeller performances, flow behaviours, and propeller scale effect behaviours. Such is their potential that it is still an on-going area of investigation in many places around the world. In this Thesis, the main objective is to obtain results from RANSE calculations of relevant parameters of the boundary layer in a marine propeller. Two turbulence models are used to predict the performance of the marine propeller P4119, and to compare the results to the experimental data made available by Jessup in 1984. A numerical verification of the results is also made, where the uncertainty and discretization errors are estimated.

The results obtained show a very acceptable value for the uncertainty and errors made, and generally a rather good agreement of the simulated results with the experimental data available. Even though the two turbulence models yield similar but different results, the $\gamma - \tilde{R}e_{\theta_t}$ model is considered a more suitable model for this work, since it includes both a laminar and a turbulent region, with the transition region present. The $k - \omega$ SST model is considered not as good for the case studied in this Thesis.

Keywords: Turbulence and transition model, Marine propeller, RANSE, Simulation

Contents

List of Tables

List of Figures

Nomenclature

$\alpha_1, \beta_1, \sigma_k, \sigma_\omega, \alpha_2, \beta_2, \sigma_{k2}, \sigma_{\omega 2}, a_1$ Turbulence model constants.

$\bar{q}$ Averaged quantity of a flow.

β^* Turbulence model constant.

$\mathbf{v}$ Velocity vector.

Δp Total pressure loss.

δ Boundary layer thickness.

δ^* Boundary layer displacement thickness.

δ_{ij} Kronecker symbol.

γ Intermittency.

$\gamma(\mathbf{x}, t)$ Heaviside function.

λ Tip-speed ratio.

λ_θ Acceleration parameter.

μ Molecular viscosity.

μ_t Eddy viscosity.

Ω Propeller rotation speed.

ω Turbulence dissipation rate.

ρ Density.

τ_{ij} Stress tensor.

θ Boundary layer momentum thickness.

$\tilde{P}_k$ Production limiter.

$\tilde{Re}_{\theta_t}$ Transition momentum-thickness Reynolds number.

ε_{ijk} Levi-Civita symbol.

c Propeller chord at a specific r/R.

C_f Friction coefficient.

C_p Pressure coefficient.

$c_{e1}, c_{a1}, c_{e2}, c_{a2}, \sigma_f, c_{\theta t}, s_1$ Turbulence model constants.

D_p Propeller diameter.

f Propeller camber.

F_1, F_2 Blending functions.

f_i External forces.

H Shape factor.

h_i Typical cell size.

J Advance coefficient.

k Turbulence kinetic energy.

K_Q Torque coefficient.

K_T Thrust coefficient.

n Propeller angular speed (in rps).

P Modified static pressure.

P Propeller pitch.

p Pressure.

p_∞ Free-stream pressure.

q Arbitrary quantity of a flow.

q' Fluctuation of a quantity of a flow.

q_i Residual of a flow variable.

r/R Propeller radius fraction.

Re Reynolds number.

Re_θ Momentum-thickness Reynolds number.

Re_v Strain rate Reynolds number.

S Strain rate.

S_ij Strain rate components.

t	Time.
Tu	Turbulence intensity.
u, v, w	Velocity Cartesian components.
U_ϕ	Numerical uncertainty.
v_{ref}	Reference velocity.
v_a	Advance velocity.
V_i	Velocity components with respect to the propeller-fixed reference frame.
X_i	Coordinate components with respect to the propeller-fixed reference frame.
x_i	Cartesian coordinates.
y	Distance to the nearest wall.

Glossary

$\gamma - \tilde{R}e_{\theta_t}$ Model	Turbulence model.
$k - \omega$ SST Model	Turbulence model.
CFD	Computational Fluid Dynamics.
MARIN	Maritime Research Institute Netherlands.
NACA	National Advisory Committee for Aeronautics.
RANSE	Reynolds-Averaged Navier-Stokes Equations.
ReFRESCO	Reliable and Fast Rans Equations Code for Ships and Constructions Offshore.

Chapter 1

Introduction

Describing the world in which we live employing the use of mathematics is an action that has been repeatedly done by humanity during thousands of years. It is not insurmountable to think that we will keep doing this for a very long time after the present day. This Thesis is but a mere iteration of this action, by reproducing the experiments carried out by Stuart D. Jessup et al in 1984 [1], with two different turbulence models widely used in Marine Engineering.

This document presents the results obtained in the realization of this Master's Thesis, done at the Instituto Técnico Superior, in Lisbon, with the supervision of the professor João Manuel Costa Baltazar.

1.1 Motivation

Why would an Aerospace Engineering student want to do their thesis on a topic in Marine Engineering?, the reader may ask upon going through this document. Well, the reason is rather straightforward. Marine and Aerospace Engineering share enough similarities that a lot of topics studied in one area are applicable to the other one; aerodynamics and hydrodynamics are not so different after all. Moreover, discovering and learning how mathematics help shape our understanding of the world is a rather important knowledge to acquire, and nothing better than doing it in the last stage of my university studies.

Besides the similarities between the two areas, which definitely helped decide the topic for the thesis, one thing I had clear in my mind was that I wanted to do the thesis on any topic involving Computational Fluid Dynamics (CFD), or CFD analysis. Following what I previously said, it is very interesting to observe how the turbulence models are applied to real-world cases and describe reality with more or less fidelity, and as a result it is our work –the work of the engineer– to apply this knowledge to solve real-world problems.

This interest in watching mathematics describe real-world situations appeared when I first started learning aerodynamics during the Bachelor's Degree: I had a clear objective since then to expand my knowledge on this area in a future final work. With this in mind, I have strived to reach this goal and now

it seems I have reached it in doing this Thesis. From now on, I hope that this can be the starting point of my future career as an Aerospace Engineer.

1.2 Objectives

The main objective of this Thesis is to derive from the RANSE calculations the relevant blade boundary layer flow parameters and compare the results with the experimental data obtained by Jessup et al in 1984 [1]. Furthermore, secondary objectives of this work include:

1. Do a literature review on the boundary layer flow on marine propeller blades.
2. Calculate the flow around the propeller P4119, with RANSE code REFRESCO including the effect of transition.
3. Estimate the numerical errors that occur in the simulations.
4. Analyse the propeller blade flow, as well as the parameters of the boundary layer.
5. Gain a deeper understanding of the physics of the flow from the results obtained.

1.3 Thesis Outline

This Thesis has seven chapters. The first and current one is the Introduction, in which a brief summary on the topic and objectives of the Thesis is made. After this, Chapter 2 presents the literature review of the topic, covering some of the recent investigations carried out on turbulence models for marine and aerospace applications. Chapter 3 covers the mathematical aspects of the Thesis, such as the RANS equations and an explanation of the turbulence models employed in the simulations.

Chapter 4 deals with the simulation setup, and explains the different grids used, the nature of the solving tool used as well as the boundary conditions applied. Chapter 5 analyses the numerical errors obtained in the simulations and whether or not they are reliable, numerically speaking; Chapter 6 compares the simulation results with the experimental data, and Chapter 7 sums up the conclusions extracted from the previous chapters. Following that, Annex A provides an example of a control file for the simulations, and Annex B contains different residuals graphics for all the simulated cases not included in the main body of the Thesis.

Chapter 2

State of the Art

In recent times, turbulence modelling and prediction has been a topic of importance in both Marine and Aeronautical Engineering. Real world turbulence has also very well studied effects on aeronautical and marine equipment. This chapter aims to shed a light on the investigations and studies carried out in these fields.

2.1 Investigation in turbulence modelling in Marine Engineering

There are several areas of investigation regarding turbulence models in Marine Engineering. The first one addressed is the one that suggests modifications to already existing turbulence models. For instance, in the Fifth International Symposium on Marine Propulsors, Moran-Guerrero et al [2] studied the modification of the $\gamma - \tilde{Re}_{\theta_t}$ model that included crossflow effects. The newly modified model was compared to the conventional $\gamma - \tilde{Re}_{\theta_t}$ model and the fully turbulent $k - \omega$ SST model for three different propellers. The results showed clearly that the new model improved the results obtained in most cases, which shows the importance of taking into account crossflow effects.

A few years later, Yao and Zhang [3] used the $\gamma - \tilde{Re}_{\theta_t}$ model to study the effects that the inflow Reynolds number (Re), the turbulence intensity (I) and the pressure gradient all have on the transition Reynolds number (Re_T) and the transition location (P_T) . They found that both Re_T and P_T depend strongly on Re, I, and the pressure gradient; they also concluded that Re_T varies along the blade sections of the same propeller. In the end they proposed a simple method for estimating P_T based on propeller geometry and the advance coefficient.

Of course, the main purpose of turbulence models is to predict flows and propeller characteristics and other phenomena. Wang and Walters [4] carried out simulations of a marine propeller using two different turbulence models: a transition-sensitive model and a fully turbulent model. The results of the study showed that the transition-sensitive model calculated better blade-surface stresses, flow separations and tip-vortex originations, which contribute to better predict propeller performance. The final

conclusion was that the transition-sensitive model is practical and effective to predict 3D flows on complex geometries in high-load simulations.

Some years later, in 2018, Helal et al [5] studied the simulation of a cavitating 3D flow on marine propellers using mainly the $k - k_l - \omega$ transition-sensitive model, and using the standard $k - \varepsilon$ model for comparison. The results were later compared to experimental data available in the literature. The authors found that, for lower rotational speeds (i.e. lower reynolds numbers), the $k - k_l - \omega$ model had a better agreement with experimental data, and at higher Reynolds numbers, the fully turbulent $k - \varepsilon$ worked better. The final conclusion was that the proposed CFD simulation procedure was a reliable and efficient way to predict cavitation, as well as the performance characteristics of a marine propeller under cavitation.

Following the prediction uses of the turbulence models, the other area in which these models stand out is in scale effects prediction. Stainer [6] described in 1998 a method employing the Reynolds Averaged Navier-Stokes method (RANS) that could be used to predict the performance of performance of marine propellers based on their size, also called the scale effects. This method also included both a pre-processing and a post-processing capability, and used the P4119 propeller, among others to compare the data obtained with the experimental one.

From 2009, the International Symposiums on Marine Propellers were held around the globe, and some of them held conferences which approached the topic of scale effects on marine propellers. On the first Symposium, Krasilnikov et al [7] investigated the scale effects on propellers with different magnitude of skew in turbulent flow. They found, among other things, that scale effects on open water characteristics depended on geometry and propeller loading. In 2015, Rijpkema [8] performed full-scale performance predictions based on model-scale experiments. The number of Reynolds studied ranged from 10^4 to 10^7, with the $k - \omega$ and $k - \sqrt{k}L$ models used. The results showed low numerical uncertainty and higher errors for higher advance ratios. As for the predictions made, variation of Reynolds numbers showed increase of thrust and decrease in torque for increasing Re numbers.

That same year, Bhattacharyya et al [9] studied the scale effects produced on the open water characteristics of a marine propeller. The investigation proposed to study the influence of water duct designs on the duct flow characteristics, as well as the blade and duct forces in both the model and the full-scale conditions. Using three different ducts for comparison, the authors found that the scale effects for the thrust and torque were in a comparable range for all three ducts studied. Furthermore, it was found that using a transition model for the flow, compared to fully turbulent models, showed a better correspondence with the flow predicted by CFD in the model propeller and the real flow observed from paint tests in the model-scale.

Another investigation that studied scale effects presented in these Symposiums was carried out by

Shin and Andersen in 2017 [10]. The investigation consisted in the open-water analysis of tip-modified and conventional propellers using both model scale and full scale propellers. The model scale computations were made with a transition turbulence model, while the full-scale computations were done with a fully turbulent model. The authors concluded that, for the tip-modified propellers, the efficiency gain is increased at full scale. They also concluded that the effects of laminar and transitional flows are crucial for model-scale propellers.

Regarding the investigation on modelled turbulent flows, Gaurier et al [11] studied the interactions between three horizontal axis turbines, in three different configurations, so as to understand the interaction effects these turbines have and apply it later in the design of marine current arrays. This study was done for different ambient turbulence intensity rates, which affects the wake of the turbines and its later dissipation. The results vary greatly for all three configurations, except that the downstream wake did not seem to be affected by the two upstream wakes, which was common in all three configurations. In the end, the conclusion was that some configurations allowed for more densely populated arrays, but it all depended on the ambient turbulence intensity.

Lastly, an investigation by Togneri et al studied the influence of turbulence in tidal energy converters, since it affects both the peak loads they experience and their fatigue life [12]. The authors studied blade element momentum theory applied to flume-scale (i.e. small scale) tidal energy converters subject to a specific kind of *computational* flow, which is not a physical flow but provides some useful properties of real turbulence, and it is computationally cheap to reproduce compared to other flows. The results obtained by the investigators showed that the variability of turbine loads has a straightforward relationship to the turbulence intensity of the inflow.

2.2 Investigation in turbulence modelling in Aeronautical Engineering

In the field of Aeronautical Engineering there are also areas of investigation regarding turbulence modelling and prediction. Investigations in turbulence models have also studied how to modify existing models to improve the predictions that they do. In this sense, Rocha et al [13] performed a calibration study for the $k-\omega$ SST (shear stress transport) model, using two different NACA Airfoils for small scale wind turbines. The parameter that was to be calibrated was the β^*, which is the turbulence modelling constant. Several values for this parameter were tested with different tip-speed ratios (λ), and the results showed that this model could accurately be used for the simulation of small-scale wind turbines.

Following other modifications in the $k-\omega$ SST model, an investigation done by Bouras et al [14] studied how to modify the model to accurately predict the recovery of wind wakes in wind turbines . The

authors suggested modifications in the aforementioned model to achieve zero streamwise gradient for all the fluid flow variables in neutral atmospheric flows. They tested this model in different speeds and turbulence levels. The results obtained showed a good match between the experimental data and the computational simulations, but only for high thrust coefficients— otherwise, the agreement in the data was poor at best.

Moving on to more recent investigations, D'Alessandro et al [15] developed a tool to compute flow parameters of wind blade airfoil sections, thus reducing the necessity for wind tunnel testing, which is known for being costly. The approach employed included performing CFD calculations using a laminar-to-turbulent transition model with a RANS-based approach— the $\gamma - \tilde{Re}_{\theta_t}$ technique with the Spalart–Allmaras turbulence model. This approach can model transitional flows at relatively low computational cost. In the end, the investigation found that the S-A model offers quite reliable results for external flow applications, especially in predicting airfoil performance, including the stall region. It also showed even lower computational cost compared to the $k - \omega$ SST model.

During the last decade, the turbulence models studied in this thesis have also been object of study in other investigations. For instance, Sicot et al [16] investigated in 2008 the effect of the rotation and turbulence effects on wind aerodynamics. The results of the study showed that the freestream turbulence level has an influence on the separation point position: if the incoming flow turbulence increases, the separation point is pushed back closer to the trailing edge of the turbine blade. On the other hand, rotation of the blade did not seem to have any significant effects on the separation point location. In the end, the authors concluded that further experiments were needed to understand the behaviour of three-dimensional flow fields on blades, especially for unsteady aerodynamics.

A comparative analysis made by Razaeiha et al [17] wanted to study how different turbulence models, namely modified $k-\omega$ SST models with different number of equations and transition models, predict the flow characteristics on a vertical axis wind turbine, provided that the experimental data was already available. They found that for all the models tested, no different values were obtained for measured magnitudes, and that all models failed to predict experimental wake asymmetry observed in the experimental results. In terms of predictability, no model seemed to be superior than the other, but, generally, SST model variants were generally the most accurate.

The investigation conducted by A. Rona et al [18] studied the three-dimensional flow separation in a wing-body junction as a problem to be approached since its simulation is very complex. This is why the authors proposed a hybrid RANS model that uses the $k-\omega$ SST model combined with the one equation sub-grid-scale (SGS) model, and found that this hybrid model is capable of capturing flow effects that hadn't been captured before. The authors concluded that hybrid methods and models like this one can be used in non-conventional ways to obtain new results clearly not obtained before.

Another investigation that employed a hybrid model, this time the $\gamma - \tilde{Re}_{\theta_t}$ model combined with the Spalart–Allmaras model is very recent and was carried out by Rizzo et al [19]. The hybrid model is used because it has lower computational cost compared to the $k - \omega$ SST model. The objective of this investigation is to show the importance in considering transition effects in bluff body aerodynamics—specifically, in a bridge section. The results obtained in the investigation show that the model used has a particularly good agreement with the experimental data, even though the completely turbulent model (and not the transition model) seems to be able to capture the behaviour for the whole model. On the other hand, the transition model predicts the critical flutter speed closer to the experimental value in comparison to the fully turbulent model.

Chapter 3

Mathematical Models

In this chapter, the equations that will be used to solve the flow around the propeller will be discussed. Two different turbulence models that complement said equations are to be discussed as well– the $k-\omega$ SST Model, a model that assumes that the flow is turbulent[1], and the $\gamma - \tilde{Re}_{\theta_t}$ Model, which combined with the $k-\omega$ SST Model takes into account the effect of transition from laminar to turbulent flow.

3.1 The Reynolds-Averaged Navier-Stokes equations

The equations that are going to be solved are the Reynolds-Averaged Navier-Stokes (RANS) equations. These are obtained by applying the Reynolds decomposition to the Navier-Stokes equations, which will be briefly discussed in following subsections.

3.1.1 The Navier-Stokes equations

The Navier-Stokes equations are a set of equations that describe the general motion and behaviour of a flow. Though there are three equations in the set, i.e. continuity, momentum and energy, only the first two are usually considered when heat exchange is not an important part of the flow solution, and the overall total energy change is not significant. Following that, the equations of continuity and momentum are presented below, in the tensor notation, in Cartesian coordinates [20]:

$$\frac{\partial \rho}{\partial t} + \frac{\partial(\rho u_i)}{\partial x_i} = 0 \tag{3.1}$$

$$\frac{\partial(\rho u_i)}{\partial t} + \frac{\partial(\rho u_i u_j)}{\partial x_j} = -\frac{\partial p}{\partial x_i} + \frac{\partial \tau_{ij}}{\partial x_j} + \rho f_i \tag{3.2}$$

in which ρ is the fluid density, u_i are the velocity components, which are also described as $(u_1, u_2, u_3) = (u_x, u_y, u_z) = (u, v, w)$; the same happens with x_i, which are the coordinates: $(x_1, x_2, x_3) = (x, y, z)$. t is the time, p is the pressure, f_i are external forces and τ_{ij} is the stress tensor.

[1] The model actually considers laminar flow but it forces a regime change to turbulent very near the leading edge.

Considering that the flow to be studied in this thesis is **a)** incompressible, and **b)** steady, the term $\partial\rho/\partial t$ is equal to zero and the density can be treated as a constant. Note that this particular writing of the equations is for a fixed system, and a particular writing for the equations considering a rotating frame will be given in subsection 3.1.3.

3.1.2 Reynolds decomposition

The Reynolds decomposition is a common method for describing turbulent flows. It consists in decomposing any flow quantity into two values, the average value and the fluctuation. Mathematically, it can be described, for a quantity q [21], as

$$q = \overline{q} + q' \tag{3.3}$$

where $\overline{q}$ is the averaged value of the quantity q, and q' is the fluctuation from that average value, or the turbulence value in the case of this thesis. Simultaneously, the averaged value of the quantity is defined as

$$\overline{q}(x_i) = \lim_{T\to\infty} \frac{1}{T} \int_0^T q(x_i, t)\, \mathrm{d}t \tag{3.4}$$

in which T is a time interval that must be large compared to the typical time scale of the fluctuations [22]. This is later applied to the Navier-Stokes equations, which will result in the RANS equations as seen in the next subsection.

3.1.3 RANS equations

As previously commented, the RANS equations are obtained by applying the Reynolds decomposition to the Navier-Stokes equations. What this does is that all unsteadiness of the flow is regarded as part of the turbulence [22]. Furthermore, averaging gives rise to previously non existent terms that must be modelled; this leads to the proposal of turbulence models, discussed later in this chapter.

To obtain the RANS equations, the continuity equation (3.1) and the momentum equation (3.2) must be time averaged as defined by equation (3.4), which yields the following averaged equations:

$$\frac{\partial(\rho\overline{u_i})}{\partial x_i} = 0, \tag{3.5}$$

$$\frac{\partial(\rho\overline{u_i})}{\partial t} + \frac{\partial}{\partial x_j}\left(\rho\overline{u_i}\;\overline{u_j} + \rho\overline{u_i'u_i'}\right) = -\frac{\partial\overline{p}}{\partial x_i} + \frac{\partial\overline{\tau}_{ij}}{\partial x_j}, \tag{3.6}$$

where $\rho\overline{u_i'u_j'}$ is a new term called Reynolds stresses. A property of this new stress is the turbulence kinetic energy k, [21], defined as

$$k = \frac{1}{2}\overline{u_i'u_i'}. \tag{3.7}$$

On the other hand, $\overline{\tau}_{ij}$ are the mean viscous stress tensor components, defined as

$$\overline{\tau}_{ij} = \mu \left(\frac{\partial \overline{u_i}}{\partial x_j} + \frac{\partial \overline{u_j}}{\partial x_i} \right) \tag{3.8}$$

where μ is the fluid's dynamic viscosity.

Let us consider now the Bousinessq hypothesis, which approximates the Reynolds stress as an increased viscosity [22]:

$$\tau_{ij} = \mu_t \left(\frac{\partial \overline{u_i}}{\partial x_j} + \frac{\partial \overline{u_j}}{\partial x_i} \right) - \frac{2}{3} \rho k \delta_{ij} \tag{3.9}$$

where μ_t is the eddy viscosity, and δ_{ij} is the Kronecker symbol[2]. If the modified static pressure as $P = p + 2/3\rho k$ is considered, the equations become

$$\frac{\partial(\rho \overline{u_i})}{\partial x_i} = 0, \tag{3.10}$$

$$\frac{\partial(\rho \overline{u_i})}{\partial t} + \frac{\partial}{\partial x_j} \left(\rho \overline{u_i}\ \overline{u_j} \right) = -\frac{\partial \overline{P}}{\partial x_i} + \frac{\partial}{\partial x_j} \left[(\mu + \mu_t) \left(\frac{\partial \overline{u_i}}{\partial x_j} + \frac{\partial \overline{u_j}}{\partial x_i} \right) \right], \tag{3.11}$$

where f_i have been disregarded. Now, to obtain the specific equations for the case to be solved in this thesis, a non-inertial reference frame fixed in the propeller must be considered [23]. The propeller rotates at a fixed speed Ω, and the flow is steady, which yields[3]

$$\frac{\partial(\rho V_i)}{\partial X_i} = 0, \tag{3.12}$$

$$\rho \frac{\partial(V_i V_j)}{\partial X_j} + \rho 2 \varepsilon_{ijk} \Omega_j V_k + \rho \varepsilon_{ipq} \varepsilon_{qjk} \Omega_p \Omega_j X_k = -\frac{\partial P}{\partial X_i} + \frac{\partial}{\partial X_j} \left[(\mu + \mu_t) \left(\frac{\partial V_i}{\partial X_j} + \frac{\partial V_j}{\partial X_i} \right) \right] \tag{3.13}$$

Because of the non-inertial frame, velocities are now written with respect to the propeller-fixed reference frame and noted as V_i, and ε_{ijk} is the Levi-Civita symbol[4]. The coordinates X_i indicate now that they are referred to the non-inertial system. To eliminate the centripetal acceleration term $\rho \varepsilon_{ipq} \varepsilon_{qjk} \Omega_p \Omega_j X_k$ in the left side of equation (3.13), the velocities $U_i = V_i + \varepsilon_{ijk} \Omega_j r_k$ are defined with respect to the inertial earth-fixed reference frame, so that it is possible to write the RANS equations [23] as

$$\frac{\partial U_i}{\partial X_i} = 0, \tag{3.14}$$

$$\rho \frac{\partial(V_j U_i)}{\partial X_j} + \rho \varepsilon_{ijk} \Omega_j U_k = -\frac{\partial P}{\partial X_i} + \frac{\partial}{\partial X_j} \left[(\mu + \mu_t) \left(\frac{\partial U_i}{\partial X_j} + \frac{\partial U_j}{\partial X_i} \right) \right]. \tag{3.15}$$

which are the equations that are ultimately going to be solved in the calculations. Note that the equations

[2]The Kronecker symbol is similar to the Levi-Civita symbol, and is defined by

$$\delta_{ij} = \binom{a}{0} = \begin{cases} 1 & \text{if } a = \pm 1, \\ 0 & \text{otherwise.} \end{cases}$$

[3]Assuming that all the flow variables are averaged over time, the $\overline{u}_i$ notation is simply written without overlines now on.

[4]The Levi-Civita symbol represents the sign of a permutation of the natural numbers 1,2, and 3, as defined by [24]:

$$\varepsilon_{ijk} = \begin{cases} +1 & \text{if } (i,j,k) \text{ is (1,2,3), (2,3,1) or (3,1,2),} \\ -1 & \text{if } (i,j,k) \text{ is (3,2,1), (1,3,2) or (2,1,3),} \\ 0 & \text{if } i = j, \text{or } j = k, \text{or } k = i \end{cases}$$

are written in a non-inertial reference system, but the unknown velocity is referred to a fixed frame.

3.2 The $k-\omega$ Shear Stress Transport model

3.2.1 Background

The $k-\omega$ Shear Stress Transport model ($k-\omega$ SST or just SST) was originally proposed by F.R Menter in 1994 [25], and was born out of experience of the author in comparing different already existing models at the time and test data obtained in experiments, namely the $k-\varepsilon$ and the $k-\omega$ models. This *new* model is based on these already existing models with, of course, some modifications.

The model used in this thesis, though, is a modified version of this model proposed by Menter et al in 2003 [26], almost ten years after its original publication. This modification came motivated because of the usage of the model beyond the field of aerodynamics it was conceived in, and "the need for accurate computations of flows with pressure-induced separation goes far beyond aerodynamics" (p. 625). It will be described in the following subsection.

3.2.2 Model formulation

The $k-\omega$ SST model is a two-equation model to determine the kinetic turbulence energy, k, and rate of turbulence dissipation, ω. The model also assumes that the flow is turbulent, even though it actually forces a regime change in the flow as near as possible to the leading edge.

The two equations that define the model are presented below[5] [26]:

$$\frac{\partial(\rho k)}{\partial t}+\frac{\partial\left(\rho U_i k\right)}{\partial x_i}=\tilde{P}_k-\beta^*\rho k\omega+\frac{\partial}{\partial x_i}\left[\left(\mu+\sigma_k\mu_t\right)\frac{\partial k}{\partial x_i}\right], \tag{3.16}$$

$$\frac{\partial(\rho\omega)}{\partial t}+\frac{\partial\left(\rho U_i \omega\right)}{\partial x_i}=\alpha\rho S^2-\beta\rho\omega^2+\frac{\partial}{\partial x_i}\left[\left(\mu+\sigma_\omega\mu_t\right)\frac{\partial\omega}{\partial x_i}\right]+2(1-F_1)\rho\sigma_{\omega 2}\frac{1}{\omega}\frac{\partial k}{\partial x_i}\frac{\partial\omega}{\partial x_i}, \tag{3.17}$$

A production limiter $\tilde{P}_k$ in equation (3.16) is used in this model. Its function is to prevent the build up of turbulence in stagnation regions, and is defined as

$$\tilde{P}_k=\min\left(P_k, 10\beta^*\rho k\omega\right), \tag{3.18}$$

with

$$P_k=\mu_t\frac{\partial U_i}{\partial x_j}\left(\frac{\partial U_i}{\partial x_j}+\frac{\partial U_j}{\partial x_i}\right). \tag{3.19}$$

In the same equation, the term $\beta^*\rho k\omega$ is called the destruction term, and does the opposite job as the production limiter.

[5] Even though the time term was included in the equations for the sake of the model, the author wants to remind the reader that these terms are not to be employed in later calculations.

On the other hand, F_1 in equation (3.17) is a blending function defined by

$$F_1 = \tanh\left\{\left\{\min\left[\max\left(\frac{\sqrt{k}}{\beta^*\omega y}, \frac{500\mu}{y^2\omega}\right), \frac{4\rho\sigma_{\omega 2}k}{CD_{k\omega}y^2}\right]\right\}^4\right\}, \tag{3.20}$$

being y the distance to the nearest wall and $CD_{k\omega} = \max\left(2\rho\sigma_{\omega 2}\frac{1}{\omega}\frac{\partial k}{\partial x_i}\frac{\partial \omega}{\partial x_i}, 10^{-10}\right)$.
S, also in equation (3.17), is the strain rate, defined as

$$S = \sqrt{2S_{ij}S_{ij}}, \text{ with } S_{ij} = \frac{1}{2}\left(\frac{\partial U_i}{\partial x_j} + \frac{\partial U_j}{\partial x_i}\right) \tag{3.21}$$

which is one of the modifications proposed by the authors. This also affects the definition of the eddy viscosity, which uses the strain rate:

$$\mu_t = \frac{\rho a_1 k}{\max(a_1\omega, SF_2)}. \tag{3.22}$$

In the same way as F_1, F_2 is a blending function given by

$$F_2 = \tanh\left\{\left[\max\left(\frac{2\sqrt{k}}{\beta^*, \omega y}, \frac{500\mu}{\rho y^2\omega}\right)\right]^2\right\}. \tag{3.23}$$

3.2.3 Model constants

The model uses a series of constants, presented in Table 3.1 below. Some of these constants do not appear in the mathematical formulation because they are used to calculate other constants. All constants are computed by a blend from the corresponding constants of the $k-\varepsilon$ and the $k-\omega$ model: for instance, the constant α is calculated as $\alpha = \alpha_1 F + \alpha_2(1-F)$ [23], and the same happens with β, σ_k and σ_ω.

Table 3.1: The $k-\omega$ SST Model constants.

Constant	β^*	α_1	β_1	σ_k	σ_ω	α_2	β_2	σ_{k2}	$\sigma_{\omega 2}$	a_1
Value	0.09	5/9	3/40	0.85	0.5	0.44	0.0828	1	0.856	0.31

3.3 The $\gamma - \tilde{\mathrm{Re}}_{\theta_\mathrm{t}}$ Model

3.3.1 Background

This model, which is also called the $\gamma - \tilde{Re}_{\theta_t}$ correlation-based transition model, was proposed by Langtry and Menter in 2009 [27], as a result of the observations made by the authors that the effect of laminar to turbulent flow transition was not included in engineering CFD simulations at the time. Moreover, the authors were preoccupied with conventional RANS procedures, which at the time did not allow for the easy description of transitional flows.

The idea behind this model was to use Van Driest and Blumer's vorticity Reynolds number [28] as a link between the Reynolds number and the local boundary layer quantities. In that regard, the strain rate Reynolds number is defined as

$$Re_v = \frac{\rho y^2}{\mu} S \tag{3.24}$$

where y is the distance from the nearest wall. By scaling Re_v to have a maximum of 1 inside the boundary layers, the authors found that it relates to the momentum-thickness Reynolds number as

$$Re_\theta = \frac{\max(Re_v)}{2.193}. \tag{3.25}$$

This relationship serves as one of the basis for the formulation of the model.

3.3.2 Model equation I: Intermittency

Intermittency is a local magnitude that can be understood as a factor of mixing between two kinds of flow– that is, in a certain point on a flow, it is sometimes turbulent and sometimes non-turbulent, making it intermittent [29]. Quantitatively, it can be described in terms of the unit function, or Heaviside function, as

$$\gamma(\mathbf{x}, t) = H(|\omega(\mathbf{x}, t)| - \omega_{\mathrm{thresh}}), \tag{3.26}$$

where ω_{thresh} is a small, positive threshold. The model proposes an equation for the intermittency [27] as follows:

$$\frac{\partial(\rho\gamma)}{\partial t} + \frac{\partial\left(\rho U_j \gamma\right)}{\partial x_j} = P_\gamma - E_\gamma + \frac{\partial}{\partial x_j}\left[\left(\mu + \frac{\mu_t}{\sigma_f}\right)\frac{\partial \gamma}{\partial x_j}\right]. \tag{3.27}$$

The transition source term

The term P_γ is called the transition source term, and it is defined as

$$P_\gamma = F_{\mathrm{length}}\, c_{a1} \rho S \left[\gamma F_{\mathrm{onset}}\right]^{0.5} (1 - c_{e1}\gamma) \tag{3.28}$$

where F_{length} is the transition length function, and it depends empirically on the transition momentum-thickness Reynolds number. The F_{onset} is a function that acts as a delimiter of the term, making it zero in the laminar boundary layer, before the transition Reynolds number is reached. The last term, $(1 - c_{e1}\gamma)$, is designed to limit the maximum value of the intermittency; to set it to maximum one, the constant c_{e1} is set to one [30]. Generally, this term ensures the *production* of intermittency where it is due to be, controlled by the F_{onset} function. The following equations presented help define this function for P_γ:

$$F_{\text{onset1}} = \frac{Re_v}{2.193 Re_{\theta_c}}, \tag{3.29}$$

$$F_{\text{onset2}} = \min\left(\max\left(F_{\text{onset1}}, F_{\text{onset1}}^4\right), 2.0\right), \tag{3.30}$$

$$R_T = \frac{\rho k}{\mu \omega}, \tag{3.31}$$

$$F_{\text{onset3}} = \max\left(1 - \left(\frac{R_T}{2.5}\right)^3, 0\right), \tag{3.32}$$

$$F_{\text{onset}} = \max\left(F_{\text{onset2}} - F_{\text{onset3}}, 0\right) \tag{3.33}$$

where Re_{θ_c} is the critical Reynolds number where the intermittency first starts to increase in the boundary layer. It is related empirically to the transition Reynolds number $\tilde{Re}_{\theta_t}$, which is the second pillar of the model and will be discussed in section 3.3.3. On the other hand, the function F_{length} is also dependent of $\tilde{Re}_{\theta_t}$, and the relationship is also empirical.

The destructive/relaminarization source term

The term E_γ in equation (3.27) is called the destructive/relaminarization source. It is defined as

$$E_\gamma = c_{a2}\rho\Omega\gamma F_{\text{turb}}\left(c_{e2}\gamma - 1\right) \tag{3.34}$$

where Ω is the vorticity magnitude. This term acts as a sink– i.e. contrary to the function that serves the term P_γ. It ensures that the intermittency remains zero or close to zero in the laminar boundary layer. As its name suggests, it also serves the function of *relaminarizing* the flow, given that the necessary conditions for it are satisfied.

The term F_{turb} acts in a similar way as the F_{onset} term in equation (3.28): it limits the appearance of this term outside of the laminar boundary layer, and is defined by

$$F_{\text{turb}} = \exp\left[-\left(\frac{R_T}{4}\right)^4\right]. \tag{3.35}$$

3.3.3 Model equation II: Transition momentum-thickness Reynolds number

The second pillar of the $\gamma - \tilde{Re}_{\theta_t}$ model is the transition momentum-thickness Reynolds number, $\tilde{Re}_{\theta_t}$. The *tilde* indicates that it is a transported magnitude. This Reynolds number uses as the reference length the boundary layer momentum thickness which, for an incompressible, two-dimensional flow, is

defined [29] as

$$\theta = \int_0^\infty \frac{u(y)}{u_0}\left(1 - \frac{u(y)}{u_0}\right)\,\mathrm{d}y. \tag{3.36}$$

where $u(y)$ is the local velocity and u_0 is the free-stream velocity. The transport equation for the momentum-thickness Reynolds number is presented:

$$\frac{\partial(\rho\tilde{Re}_{\theta_t})}{\partial t} + \frac{\partial(\rho U_j\tilde{Re}_{\theta_t})}{\partial x_j} = P_{\theta t} + \frac{\partial}{\partial x_j}\left[\sigma_{\theta t}\left(\mu + \mu_t\right)\frac{\partial\tilde{Re}_{\theta_t}}{\partial x_j}\right] \tag{3.37}$$

The newest and relevant term of this equation is the source term $P_{\theta t}$. It is used to force the transported $\tilde{Re}_{\theta_t}$ to match the local value of Re_{θ_t} (non-transported magnitude) calculated from empirical relationships. To accomplish this, the source term is defined as

$$P_{\theta_t} = c_{\theta t}\frac{\rho}{t}\left(Re_{\theta_t} - \tilde{Re}_{\theta_t}\right)(1.0 - F_{\theta t}) \tag{3.38}$$

with t being a time scale:

$$t = \frac{500\mu}{\rho U^2} \tag{3.39}$$

The term $F_{\theta t}$ is a blending function used to allow $\tilde{Re}_{\theta_t}$ to diffuse into the boundary layer from the free-stream. It is zero in the free-stream and one in the boundary layer, and it is defined as

$$F_{\theta t} = \min\left(\max\left(F_{wake}\,\mathrm{e}^{-(y/\delta)^4}, 1.0 - \left(\frac{\gamma - 1/c_{e2}}{1.0 - 1/c_{e2}}\right)^2\right), 1.0\right) \tag{3.40}$$

where δ is the boundary layer thickness. In the model, it is obtained through the equations

$$\theta_{BL} = \frac{\tilde{Re}_{\theta_t}\mu}{\rho U}; \qquad \delta_{BL} = \frac{15}{2}\theta_{BL}; \qquad \delta = \frac{50\Omega y}{U}\delta_{BL}. \tag{3.41}$$

The F_{wake} function serves as a limiter so that the blending function is not active in the wake regions downstream of the blade, and defined as

$$F_{\mathrm{wake}} = \exp\left[-\left(\frac{Re_\omega}{10^5}\right)^2\right], \text{ with } Re_\omega = \frac{\rho\omega y^2}{\mu}. \tag{3.42}$$

To finish this subsection, there are two additional parameters that influence the beginning of the transition, calculated empirically:

$$\lambda_\theta = \frac{\rho\theta^2}{\mu}\frac{dU}{ds}, \tag{3.43}$$

$$Tu = 100\frac{\sqrt{2k/3}}{U} \tag{3.44}$$

λ_θ is the acceleration parameter, depending on the streamwise acceleration dU/ds, and Tu is the turbulence intensity.

3.3.4 Integration with the $\mathrm{k}-\omega$ SST model

The model presented up until this point is not complete. In reality, the $\gamma - \tilde{Re}_{\theta_t}$ model[6] is a four-equation model that uses the two equations presented in this section for the intermittency, equation (3.27), and the momentum-thickness Reynolds number, equation (3.37), and also the two equations from the $k-\omega$ SST model, equations (3.16) and (3.17). In that regard, there are a series of modifications that are made to the $k-\omega$ SST model that allow it to fully interact with the $\gamma - \tilde{Re}_{\theta_t}$ model. But first, a modification to the intermittency for predicting separation-induced transition must be done:

$$\gamma_{\text{sep}} = \min\left(s_1 \max\left[0, \left(\frac{Re_v}{3.235 Re_{\theta_c}}\right) - 1\right] F_{\text{reattach}}, 2\right) F_{\theta_t} \tag{3.45}$$

with $F_{\text{reattach}} = \mathrm{e}^{-(R_T/20)^4}$. Then the effective intermittency is defined as

$$\gamma_{\text{eff}} = \max(\gamma, \gamma_{\text{sep}}). \tag{3.46}$$

With this in mind, the transport equation for k (3.16) is modified to be

$$\frac{\partial(\rho k)}{\partial t} + \frac{\partial\left(\rho U_i k\right)}{\partial x_i} = \tilde{P}_k - \tilde{D}_k + \frac{\partial}{\partial x_i}\left[\left(\mu + \sigma_k \mu_t\right)\frac{\partial k}{\partial x_i}\right] \tag{3.47}$$

being the main modification done in the production term $\tilde{P}_k = \gamma_{\text{eff}} P_k$ and the destruction term $\tilde{D}_k = \min(\max(\gamma_{\text{eff}}, 0.1), 1.0) D_k$, where P_k is already defined in equation (3.19) and $D_k = \beta^* \rho k \omega$. On top of that, the blending function F_1 that appears in the ω equation (3.17) is modified as follows:

$$F_1 = \max(F_{1,\text{original}}, F_3), \tag{3.48}$$

$$F_3 = \mathrm{e}^{-(R_y/120)^8}, \tag{3.49}$$

$$R_y = \frac{\rho y \sqrt{k}}{\mu} \tag{3.50}$$

where $F_{1,\text{original}}$ is the original blending function of the model defined in equation (3.20).

3.3.5 Model constants

To end this section, and in the same way as in the previous section, Table 3.2 shows the constants and their values used in this model.

Table 3.2: The $\gamma - \tilde{Re}_{\theta_t}$ correlation-based transition model constants.

Constant	c_{e1}	c_{a1}	c_{e2}	c_{a2}	σ_f	$c_{\theta t}$	$\sigma_{\theta t}$	s_1
Value	1.09	2.0	50	0.06	1.0	0.03	2.0	2

[6] From now on, every mention of the $\gamma - \tilde{Re}_{\theta_t}$ model will be referred to the complete model.

Chapter 4

Simulations

The main topic of this thesis is performing CFD simulations using the mathematical models shown in Chapter 3. This chapter reviews the main aspects of the simulations performed, including the geometry of the propeller and the domain employed, the grids, the calculation parameters and the boundary conditions.

4.1 Overview

The simulations performed are based in the investigations carried out by Jessup et al [1] and presented in the 15th Symposium of the Office of Naval Research in Hamburg, Germany, in 1984. The goal of the simulations is to reproduce the experimental results using the two mathematical models discussed previously.

The CFD code used to perform the simulations is the Reliable and Fast Rans Equations Code for Ships and Constructions Offshore (ReFRESCO) developed within a cooperation led by the Maritime Research Institute Netherlands (MARIN). As its name says, it is a RANS-based code that considers a multi-phase flow approach, i.e. there are different fluids or species in the flow domain [31]. Furthermore, the code considers that all fluids are Newtonian, isothermal and incompressible; for the discretization it adopts the Finite Volume Method in a cell-centered, collocated arrangement. The code also implements a wide variety of turbulence and transition models to be chosen, in which the $k-\omega$ SST 2003 Model and the $\gamma - \tilde{R}e_{\theta_t}$ 2003 Model are included.

All the simulations were performed in a local computer with a 16-core processor available to the student, except the finer cases, which were calculated in a cluster owned by MARIN, available to Prof. Baltazar.

4.2 Geometry

4.2.1 Propeller

The propeller used in the simulations is the DTRC 4119 Propeller, a three-blade propeller originally designed by Denny [32]. It has a diameter of $D_p = 0.305$ m, rotates right-handed, its section thickness form is based in the NACA66 profile, has no skew or rake, and its design advance coefficient is $J = 0.833$. The advance coefficient is the ratio between the free-stream velocity that reaches the propeller and the speed of the tip of the propeller:

$$J = \frac{v_a}{nD_p} \tag{4.1}$$

where v_a is the advance velocity, n is the angular speed (in rps) and D_p is the propeller diameter. Figure 4.1 shows a schematic of the propeller. Table 4.1 below, extracted from [1], shows a summary of the geometric characteristics of the propeller P4119, where r/R is the fraction of the propeller radius, c is the chord at a specified radius, P is the pitch, t is the mean line and f is the camber.

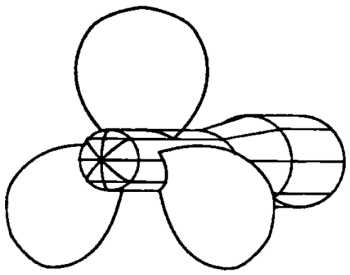

Figure 4.1: The DTRC P4119 Propeller. From [1].

Table 4.1: Geometrical characteristics of the propeller P4119. Extracted from [1].

r/R	c/D_p	P/D_p	t/c	f/c
0.2	0.320	1.105	0.20550	0.01429
0.3	0.3625	1.102	0.15530	0.02318
0.4	0.4048	1.098	0.11800	0.02303
0.5	0.4392	1.093	0.09016	0.02182
0.6	0.4610	1.088	0.06960	0.02072
0.7	0.4622	1.084	0.05418	0.02003
0.8	0.4347	1.081	0.04206	0.01967
0.9	0.3613	1.079	0.03321	0.01817
0.95	0.2775	1.077	0.03228	0.01631
1.0	0.0	1.075	0.03160	0.01175

4.2.2 Domain

The domain of study has a cylindrical shape. The propeller is located in the centre of the domain, i.e. in the mid-length of the cylinder and in the centre of its radius. Relative to the propeller diameter, its dimensions are radius $R_D = 5D_p$ and length $l_D = 10D_p$. These dimensions are chosen so that the boundaries of the domain do not have any effect on the flow that reaches the propeller– that is, that the flow that reaches the propeller is as similar as possible to a real free flow [33]. Figure 4.2 shows a visualisation of the domain and a detail of the propeller.

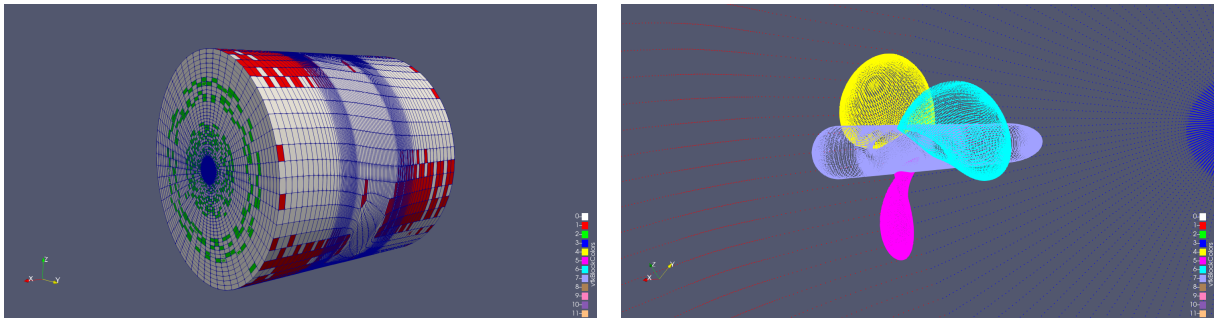

(a) The domain of study.

(b) A detail of the propeller inside the domain.

Figure 4.2: Visualisation of the domain of study.

4.3 Grids

Several grids with different number of elements have been used in the simulations, to ensure the validity of the results achieved in terms of iterative and discretization error. The grids were obtained using the software GridPro by Baltazar et al [34], and were repurposed for the simulations carried out in this Thesis. The results of the convergence study are presented in the next chapter.

A total of six grids have been used, and their characteristics are summed up in Table 4.2 below. The grid refinement ratio, which will be used in section 5.9, is also included. All of the grids are block-structured, and all of their elements are tetrahedral and hexahedron with varying sizes. Figure 4.3, extracted from [34], shows an overview of the structured grid 10M.

Table 4.2: Characteristics of the grids used.

Grid name	**Number of elements**	h_i/h_1
1M	$861,381$	3.52
2M	$1,946,304$	2.68
6M	$6,061,608$	1.83
10M	$9,946,965$	1.55
21M	$21,018,771$	1.21
38M	$37,584,261$	1.00

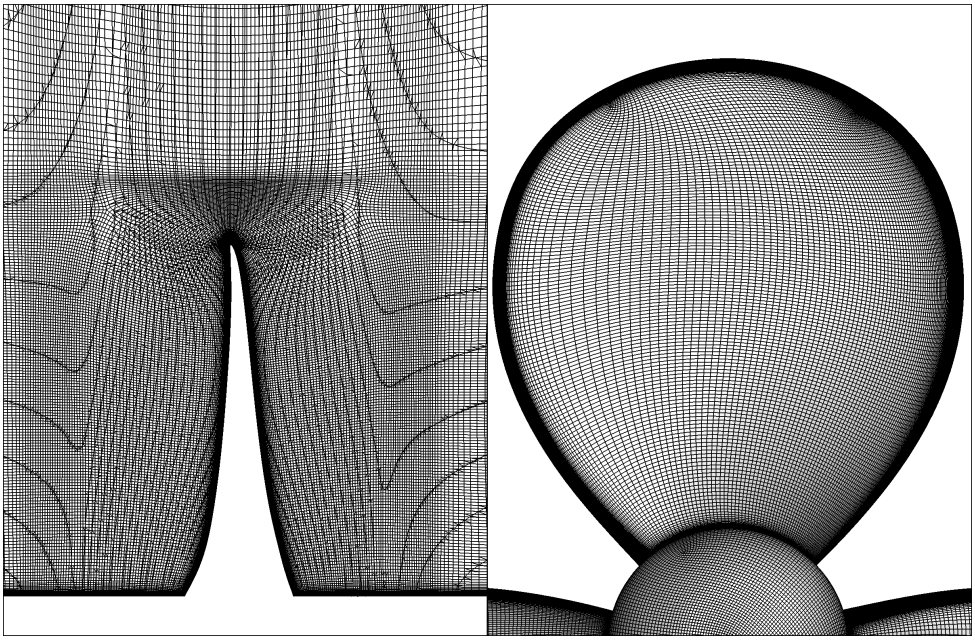

Figure 4.3: Overview of the grid 10M. From [34]

4.4 Solver and convergence

The code ReFRESCO does not solve all the equations at the same time in a unique system[1], but rather uses a segregated solution procedure, meaning that all equations are solved separately, and all the other variables are assumed to be known [35]. Every equation is solved until converged (either by reaching maximum loop iterations or reaching actual convergence criteria), and then all the equations are coupled and checked for convergence, as shown in Figure 4.4 below. To complete this section, an example control file used to prepare the simulations is shown in Appendix A.

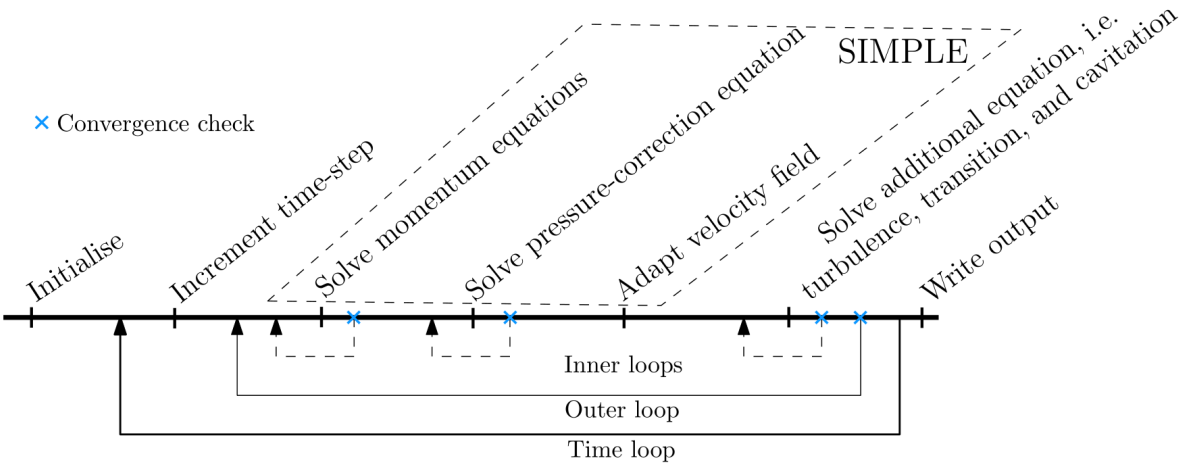

Figure 4.4: The ReFRESCO general algorithm. Extracted from [35]

As Figure 4.4 shows, ReFRESCO uses the SIMPLE algorithm to solve the momentum equation and the pressure corrections, and especially to ensure the satisfaction of the continuity equation.

Every inner loop shown in Figure 4.4 uses a different solver that suits its needs. For instance, the momentum equation uses de Generalized Minimal Residual algorithm (GMRES), proposed by Saad and Schultz [36], but the pressure correction uses the Conjugate Gradient algorithm, proposed by Hestenes and Stiefel [37]. It can also use the GMRES.

4.5 Flow parameters

For the purpose of replicating the experimental data obtained by Jessup et al, it is necessary to adjust the simulation parameters to match the conditions of the experiment. In the referred article, the authors performed the experiments at two rotational speeds, $n = 7$ rps and $n = 14$ rps. The first one is associated to a Reynolds number of $Re = 0.73 \times 10^6$ and the second one, $Re = 1.46 \times 10^6$. In addition to that, the experiment was performed at an advance coefficient of $J = 0.806$ which, remembering the definition

[1] It can solve them at the same time if the user so decides, but in this Thesis this approach was not employed.

given at equation (4.1), means that the advance velocity is set by the rest of the parameters.

Since the advance velocity is set, so is the reference velocity, which is the velocity perceived by the propeller blades at a radius $r = 0.7R$. The reference velocity is used to calculate the Reynolds number, and its value will be the Pythagorean sum of the advance velocity and the velocity of the propeller blades:

$$v_{\text{ref}} = \sqrt{v_a^2 + (2\pi n 0.7R)^2} \tag{4.2}$$

With the reference velocity set, and since the Reynolds numbers are fixed, the kinematic viscosity $\nu = \mu/\rho$ is also set. Extrapolating values for water properties, the water temperatures were obtained at around $T = 20C$. From the temperatures it was possible to obtain the desired values for the density ρ and the dynamic viscosity μ. In Table 4.3 all the parameters values used in the simulations for both Reynolds number cases are shown.

Table 4.3: Simulation parameters values.

Parameter	Units	Symbol	Case	
			$Re = 0.73 \times 10^6$	$Re = 1.46 \times 10^6$
Angular speed	rps	n	7	14
Advance velocity	m/s	v_a	1.72081	2.44162
Reference velocity	m/s	v_{ref}	5.00058	9.70246
Dynamic viscosity	$\text{Pa} \cdot \text{s}$	μ	9.601×10^{-4}	9.601×10^{-4}
Water density	kg/m^3	ρ	997.83	997.83

4.6 Boundary conditions

In this section, the specific boundary conditions used in the simulations will be discussed.

4.6.1 Inlet boundary

The inlet is the boundary in which the flow enters the computational domain. In this boundary, the pressure is then extrapolated from the value given. In the present work, the velocity was defined $\mathbf{v} = (-1.72081, 0, 0)\ \text{m/s}$[2], in an Earth fixed system, i.e. the flow velocity perceived by a fixed, external observant relative to the domain, and not the propeller. The velocity set is uniform across all the boundary.

[2]Only for the cases with the lowest Reynolds number. For the cases with the highest value, this vector would become $\mathbf{v} = (-2.44162, 0, 0)\ \text{m/s}$.

There are other variables that are also set in the inlet. For the $k-\omega$ SST model, the turbulence intensity is $Tu = 1.0\%$. Tu is also uniform across the inflow boundary, and setting it means that the turbulence kinetic energy k is also set. For the $\gamma - \tilde{Re}_{\theta_t}$ model, this value is $Tu = 1.2\%$, $Tu = 1.5\%$ and $Tu = 1.7\%$ and $\gamma = 1$ for the three cases studied. $\tilde{Re}_{\theta_t}$ is a function of k and is accordingly specified. Finally, the eddy viscosity is set to be five hundred times the molecular viscosity: $\mu_t = 500\mu$.

4.6.2 Outlet and Outer boundaries

In the outlet boundary, the condition applied is zero streamwise derivatives for all flow quantities. On the other hand, in the outer boundary a constant pressure is set and all the other variables have the Neumann condition applied to them.

4.6.3 Wall boundary

The wall boundary has special conditions applied to it compared to the other boundaries. First of all, there is a no-slip condition applied to it, which makes all velocities (u, v, w) to be zero. The second condition applied is the impermeability condition, which does not allow the flow to enter the propeller geometry. Furthermore, the pressure is set to have its derivatives be zero, k is set to be zero and ω is set according to equation (A12) in [25]. Finally, both γ and $\tilde{Re}_{\theta_t}$ have the Neumann condition applied to them.

4.6.4 Diagram

Figure 4.5 shows a diagram of the domain used in the simulations, with its dimensions and the boundaries specified in them.

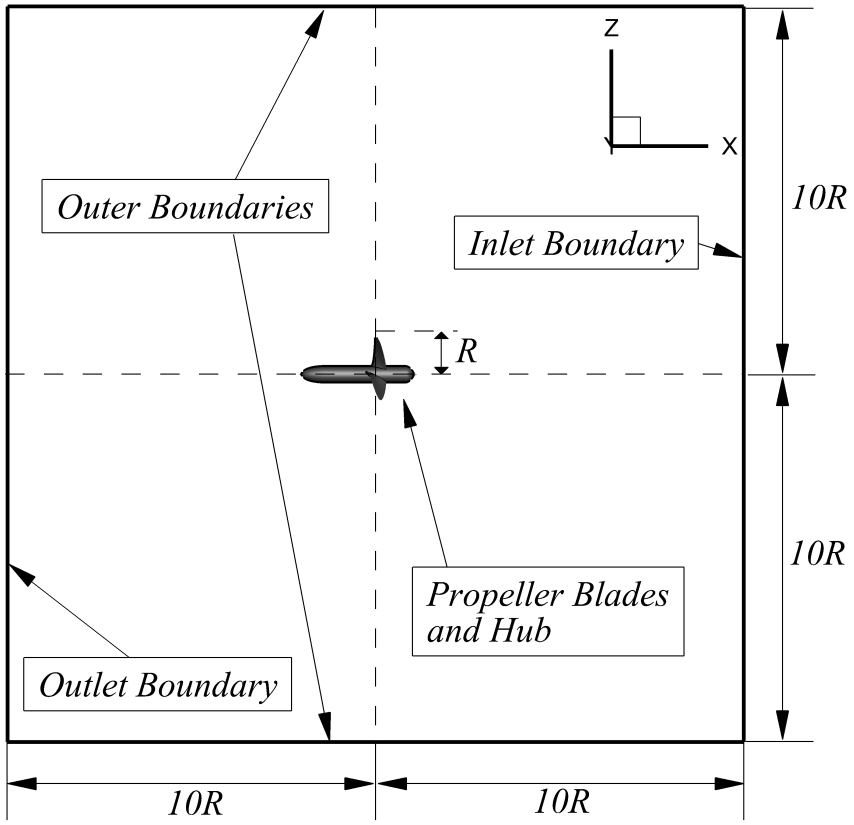

Figure 4.5: A Diagram of the domain. Extracted from [34].

Chapter 5

Numerical Verification

After having set up the simulations and all the parameters, they were run for the two turbulence models explained previously in Chapter 3, with the different grids, boundary conditions and parameters shown in Chapter 4. In this chapter, the numerical verification[1] of the results is shown. All the results shown in this chapter, unless otherwise specified, correspond –for both models– to the case $Re = 0.73 \times 10^5$, and for the $\gamma - \tilde{Re}_{\theta_t}$ model specifically, to a turbulence intensity $Tu = 1.5\%$.

5.1 Overview

When a numerical simulation is done, a process involving checking whether the results are reliable or not is carried out. For this, the terms Verification and Validation are introduced in the literature to perform this analysis. To distinguish the two, Boehm and Blottner [38, 39] define very clearly: Verification checks if the equations are being solved right, and Validation checks if the right equations are being solved. Verification is an exercise that aims to quantify the error made when solving the equations, while Validation aims to determine *"how well the mathematical model represents the world"* [40].

But when quantifying the errors in a numerical simulation, it is imperative to distinguish between three types of errors. According to Eça and Hoekstra [40], these errors are of different nature and must be treated accordingly:

- Modelling errors. These errors are a consequence of a (bad) representation of the physical world by a mathematical model. They are detected and quantified by the Validation process.
- Programming errors. These are usually found in the form of typos in the code employed to solve the mathematical model. Code Verification, not considered in this section, is responsible for reducing them.
- Numerical errors. These can be further divided into three categories, depending on its origin:

[1] It is not a complete verification since this chapter does not cover all types of errors.

- Round-off errors are related to the numerical precision of computers. For the case studied in this Thesis, with the grids used and the double precision that the computers used have, the round-off error can be disregarded.
- Iterative errors appear from the non-linearity of the equations solved in the RANS model.
- Discretization errors are a consequence of the transformation of the partial differential equations in continuum formulation into discrete formulation.

Of all the errors mentioned, this section deals with the numerical errors, which are those that correspond to the Verification process. The following section aims to check the iterative error in a qualitative way, while the last one, section 5.3, aims to quantify the discretization errors.

5.2 Iterative errors analysis

The first step in verifying the results obtained in the simulations is to perform the Iterative error analysis. This analysis is used to check how the errors generated in the numerical process evolve over the course of the simulation's analysis. The expected behaviour is that local and global parameters of the simulation, as those shown in this section, to stagnate to a certain value for the remainder of the simulation. In the following subsections certain parameters have been analysed for the convergence study.

5.2.1 Residuals

The residuals are a rather comprehensive way to understand how the general iterative error diminishes over the course of a simulation. In this section, two example plots are shown, for both models. These correspond to the calculations made with grid 38M. These graphics were obtained with the software TecPlot and show the L_2 and L_∞ residuals for several variables. These residuals are defined by

$$L_2 = \frac{\sqrt{\sum_{i=1}^{N} q_i^2}}{N} \tag{5.1}$$

$$L_\infty = \max(q_i) \tag{5.2}$$

where N is the total number of elements and q_i is the residual of a flow variable in element i.

Figure 5.1 shows the aforementioned residuals for the $k-\omega$ model. Despite some *irregularities* of the plot, like the huge increase in the residuals' value at 30.000 iterations for the turbulence dissipation (which just indicate a numerical restart of the simulation), the general trend is a decrease in the residuals' value, which indicates convergence in the calculations. The calculations stop either when maximum iterations have been reached or the residuals fall below $L < 10^{-6}$[2]. Since the latter is harder to achieve, especially in the transition model (Figure 5.2), the simulations were set up with a high number of maximum iterations to allow for the decrease in residuals even if it didn't reach the specified condition. This

[2]Since not all the residuals reached this value in a reasonable amount of iterations, the ω residual was used as a reference.

is especially true for the $\gamma - \tilde{Re}_{\theta_t}$ model, in which the residuals get oscillating around certain value as iterations go by, as shown in Figure 5.2. Graphics for other calculations made in this Thesis can be found in Appendix B.

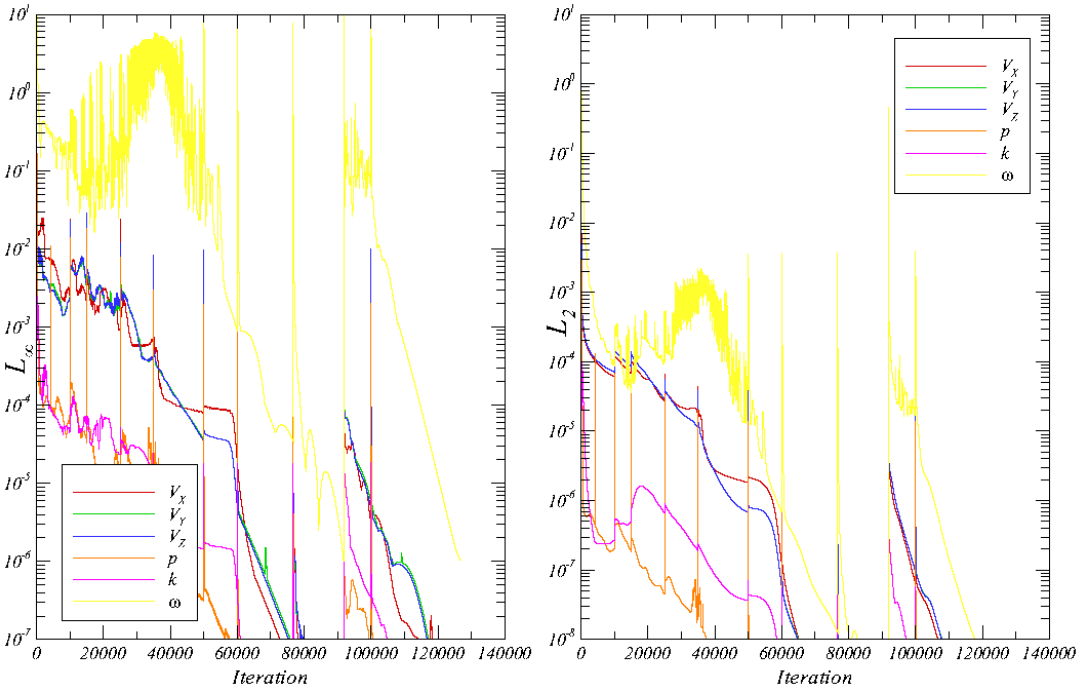

Figure 5.1: Residuals L_∞ and L_2 for the $k - \omega$ SST2003 model obtained with the 38M grid.

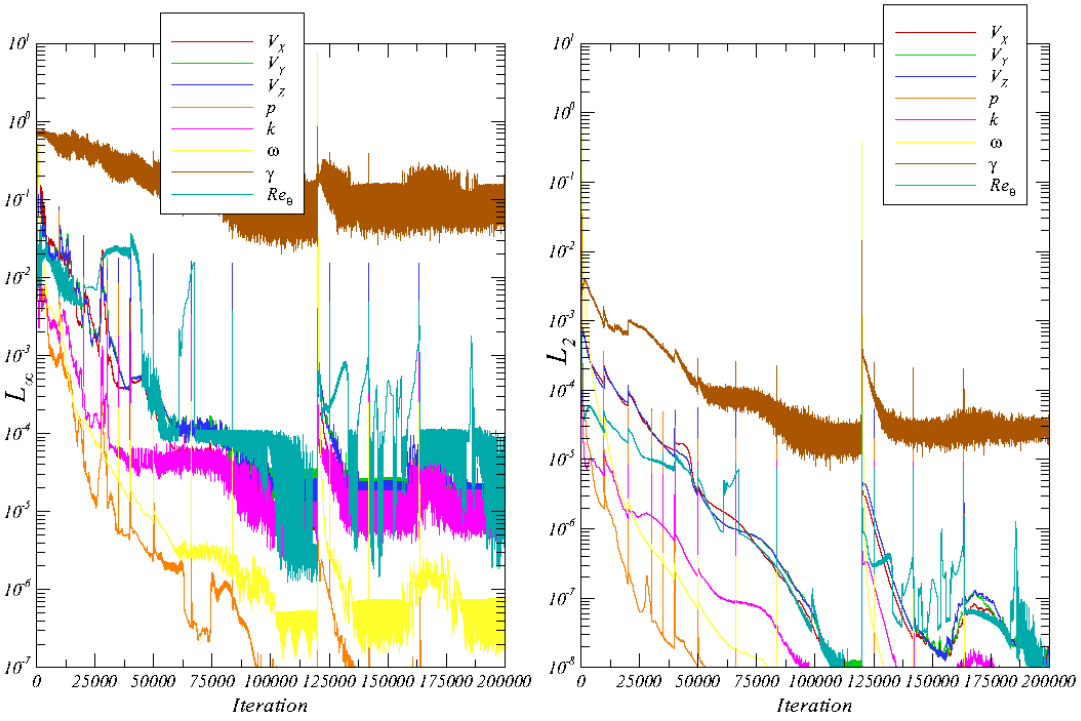

Figure 5.2: Residuals L_∞ and L_2 for the $\gamma - \tilde{Re}_{\theta_t}$ model with $Tu = 1.5\%$, obtained with the 38M grid.

5.2.2 Pressure coefficient

The pressure coefficient, defined as

$$C_p(x) = \frac{p(x) - p_\infty}{1/2\rho v_{\text{ref}}^2} \tag{5.3}$$

is a local quantity that measures the local pressure with respect to the upstream pressure and made dimensionless by the flow dynamic pressure. v_{ref} is the reference velocity, which according to Table 4.3 equals $v_{\text{ref}} = 5.00058\ \text{m/s}$ and $v_{\text{ref}} = 9.70246\ \text{m/s}$ depending on the Reynolds number of the case.

For the purpose of the iterative error analysis, the C_p has been plotted at $x/c = 0.2$ and $x/c = 0.8$ in a blade of the propeller at the radius $r = 0.7R$, versus the number of iterations performed in the simulation. The results are shown below in Figures 5.3 and 5.4.

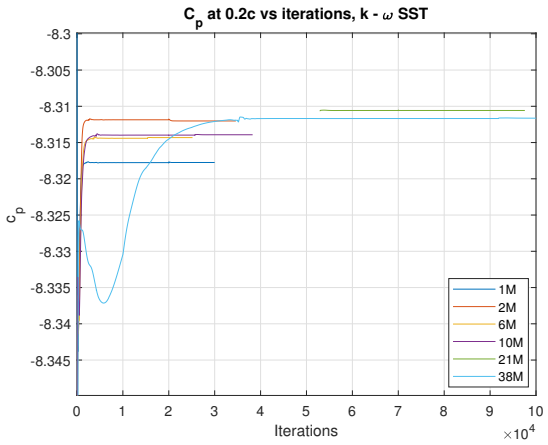

(a) The C_p at $x/c = 0.2$.

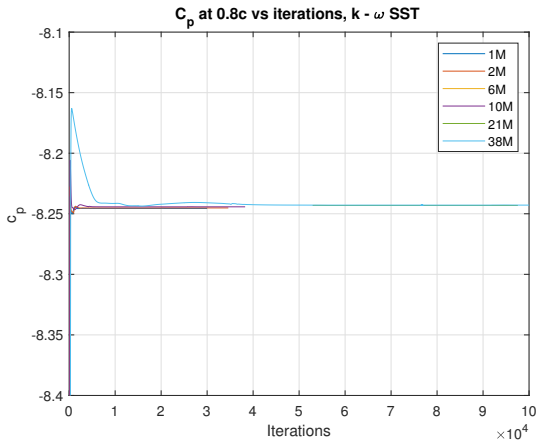

(b) The C_p at $x/c = 0.8$.

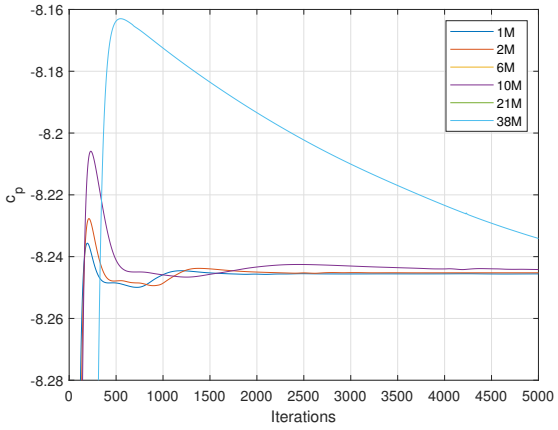

(c) A close-up of C_p at $x/c = 0.8$.

Figure 5.3: The pressure coefficient versus the simulation iterations at two points of the chord, located at the radius $r = 0.7R$, for the model $k - \omega$ SST.

The results in Figure 5.3 show that the values for the C_p stagnate rather quickly after the start of the simulation. The notable outlier is the grid 38M, which takes much longer to stagnate but eventually reaches that state. In Figure 5.3b the adjustment is much shorter iteration-wise but more exaggerated value-wise.

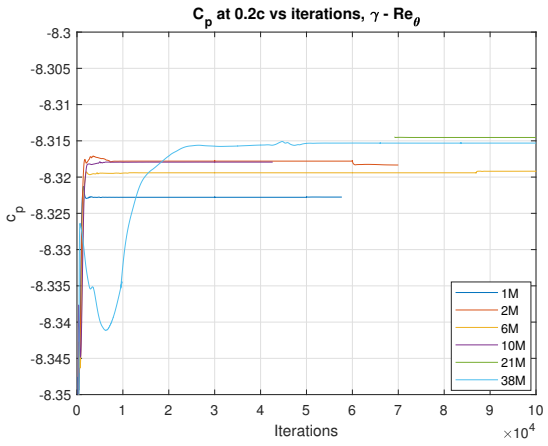

(a) The C_p at $x/c = 0.2$.

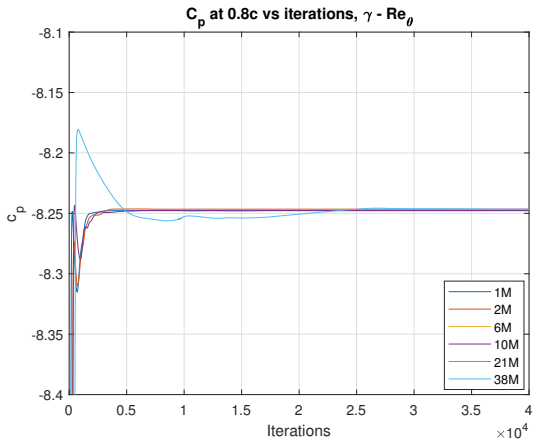

(b) The C_p at $x/c = 0.8$.

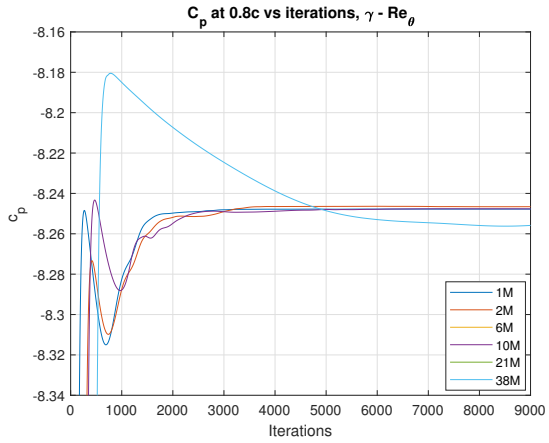

(c) A closeup of the C_p at $x/c = 0.8$.

Figure 5.4: The pressure coefficient versus the simulation iterations at two points of the chord, located at the radius $r = 0.7R$, for the $\gamma - \tilde{Re}_{\theta_t}$ model.

Regarding the $\gamma - \tilde{Re}_{\theta_t}$ model, shown in Figure 5.4, the same behaviour is encountered. C_p values quickly stagnate to a certain value, variations due to simulation restart notwithstanding. In this case, the values at x/c take longer to stagnate, about the double in number of iterations. The grid 38M again takes longer to stagnate than the other ones.

5.2.3 Thrust coefficient

The thrust coefficient, defined as

$$K_T = \frac{T}{\rho n^2 D_p^4} \tag{5.4}$$

where T is the propeller thrust, n is the angular velocity and D is the propeller diameter. This variable, contrary to the ones presented in this chapter, is a global quantity– it measures the global performance of the propeller rather than local phenomena, as seen in previous sections.

Figure 5.5 below shows the evolution of the thrust coefficient along the simulation iterations for the two models used. In both cases, there clearly is a very quick stagnation of the K_T values, with the

exception of the 38M grid. There is no notable behaviour observed.

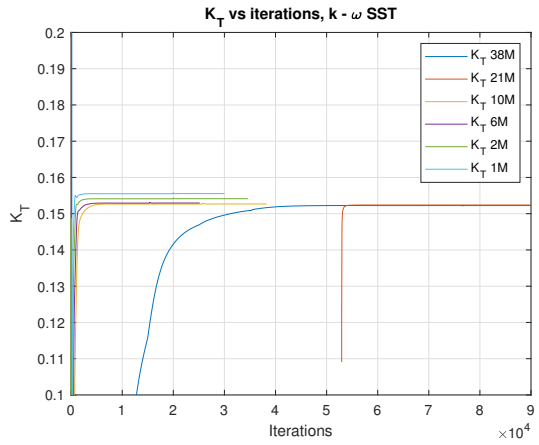

(a) Thrust coefficient vs number of iterations for the $k-\omega$ SST model.

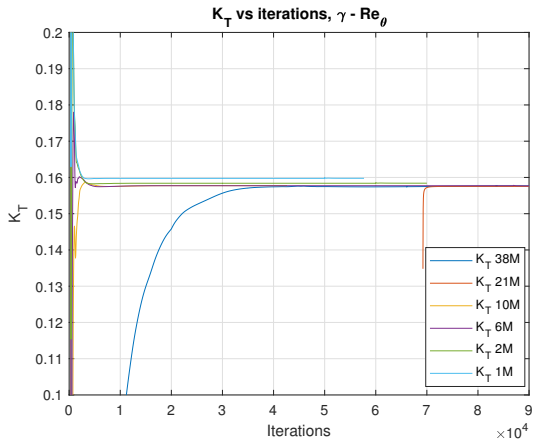

(b) Thrust coefficient vs number of iterations for the $\gamma - \tilde{Re}_{\theta_t}$ model.

Figure 5.5: The thrust coefficient versus the number of iterations of the simulation for all the grids studied and the two models used.

5.2.4 Torque coefficient

In a very similar way to the thrust coefficient, the torque coefficient is defined as

$$K_Q = \frac{Q}{\rho n^2 D_p^5}. \tag{5.5}$$

In Figure 5.6, the evolution of the torque coefficient along the simulation iterations is shown for both models used.

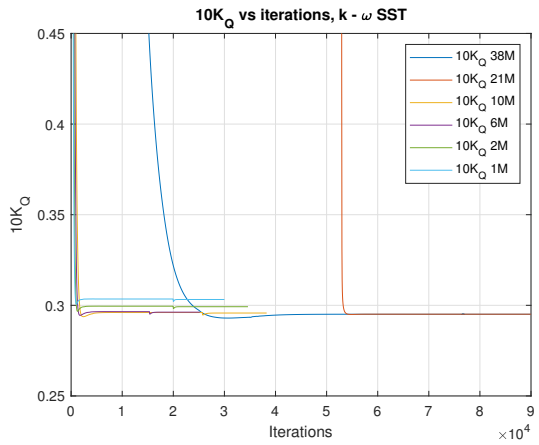

(a) Torque coefficient vs number of iterations for the $k-\omega$ SST model.

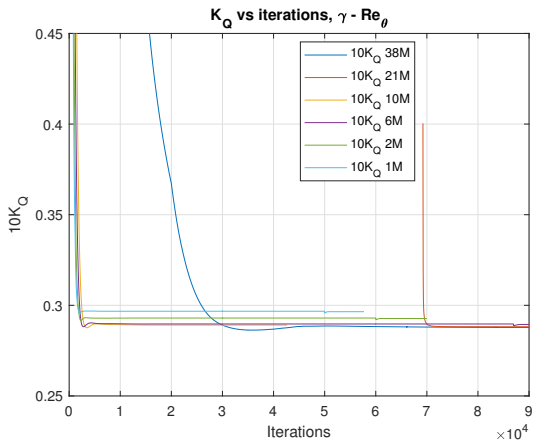

(b) Torque coefficient vs number of iterations for the $\gamma - \tilde{Re}_{\theta_t}$ model.

Figure 5.6: The torque coefficient versus the number of iterations of the simulation for all the grids studied and the two models used.

In the same way as the thrust coefficient, the torque coefficient shows rather quick stagnation in the values shown for the different grids, with –again– the exception of grid 38M.

5.3 Discretization error analysis

In the previous section, the iterative error of the results was checked for the different grids used. This section aims to perform a similar task in a general way, by assessing qualitatively the discretization in the velocity profiles and quantifying the numerical errors for select parameters, as defined in section 5.1.

5.3.1 Velocity profiles

In the same way as the previous section, the velocity profiles have been plotted for the different grids studied, at the same locations as the pressure coefficient. One should find a clear difference between the two profiles in terms of shape, showing that one profile belongs to a laminar flow and the other one to a turbulent one. Furthermore, the velocity profiles are plotted with the normal coordinate to the wall (n) divided by the chord at $r = 0.7R_p$.The profiles for the are $k - \omega$ SST model are depicted in Figure 5.7.

Figures 5.7a and b show the velocity profiles for the chord locations specified. While both profiles are different in shape, they fundamentally represent the velocity gradient for a turbulent flow. The difference in the shapes is due to flow evolution: the turbulent boundary layer gains energy when it flows along the blade chord shown in the Figure. As a result, the velocity gradients –and the velocity profiles– change as well.

Regarding the convergence of the results, the close-ups in Figures 5.7c and d show that clearly, there is no monotonic convergence, seeing that all the results from the different grids are clearly mixed, even if the general trend can be suspected (with the coarser and finer meshes in different ends of the graphic).

Looking now at the $\gamma - \tilde{Re}_{\theta_t}$ model, in Figure 5.8, the results are not that much different compared to the $k - \omega$ SST model. In what they differ is that the differences in the profiles are much more clear, in the sense that the differences between the laminar and turbulent profiles are bigger. This, of course, is only a consequence of the model itself, since it is capable of modelling both laminar and turbulent flows.

Regarding the convergence, again there is no monotonic convergence at all, and for the laminar case (Figure 5.8c) the lines corresponding to the different grids get mixed constantly. The turbulent case (Figure 5.8d) does not show this behaviour, but at the same time makes it harder to decide whether the results are converging or not.

5.3.2 Error estimation

The discretization error is usually the biggest contributor to the numerical error of a CFD solution [40], and can be easily assumed as big enough that the round-off error and the iterative error are negligible, since they are several orders of magnitude smaller. Eça and Hoekstra [41] estimate it through a truncated power series expansion in the following way:

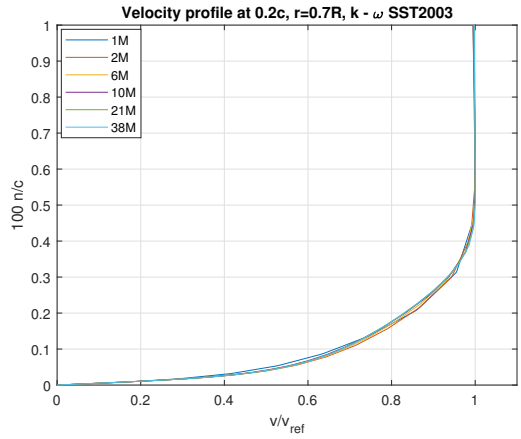

(a) Velocity profile at $x/c = 0.2$.

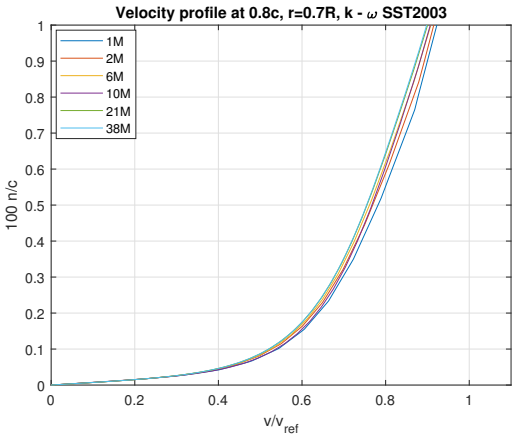

(b) Velocity profile at $x/c = 0.8$.

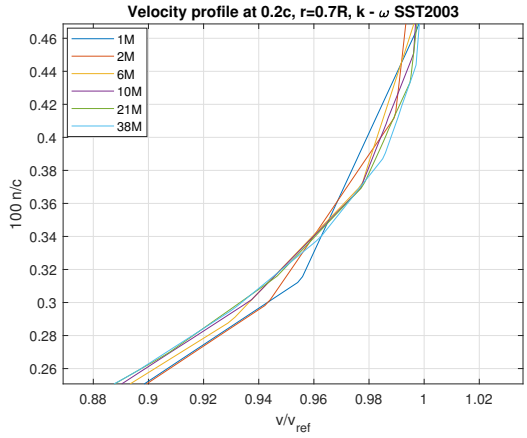

(c) Close-up of the velocity profile at $x/c = 0.2$.

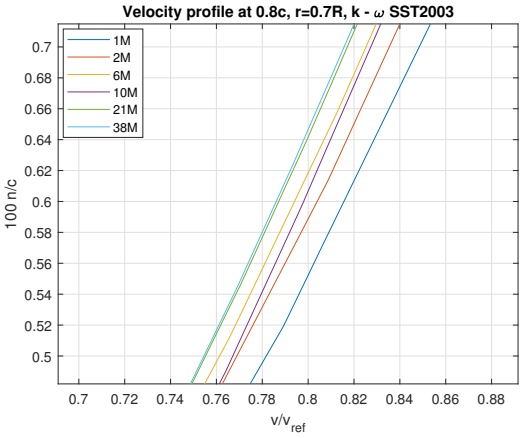

(d) Close-up of the velocity profile at $x/c = 0.8$.

Figure 5.7: Velocity profile at two points of the chord, located at the radius $r = 0.7R$, for the model $k - \omega$ SST2003.

$$\epsilon_\phi = \phi_i - \phi_0 = \alpha h_i^p \tag{5.6}$$

where ϕ_i is any integral local flow quantity, ϕ_0 is the estimate of the exact solution of the quantity, α is an unknown constant, h_i is the typical cell size of the considered grid and p is the observed order of grid convergence. Regarding the grid size, according to Baltazar et al [34], since the grids used for this Thesis *"are block-structured and the same coarsening factor is applied on each direction"*, the typical cell size of a grid i may be defined as

$$h_i = \left(\frac{1}{N_{\text{cells}}} \right)^{\frac{1}{3}} \tag{5.7}$$

which leaves the estimation of the error up to the determination of ϕ_0, α and p.

The error estimation can only be done if two assumptions are applied. The first one is that the grids must be in the "asymptotic range", that Eça and Hoekstra [40] explain as that the grid refinement ratio (i.e. h_1/h_2) is constant for the complete computational domain if the grids are geometrically similar. The second assumption is that the density of the grids is representable by a single parameter: the typical

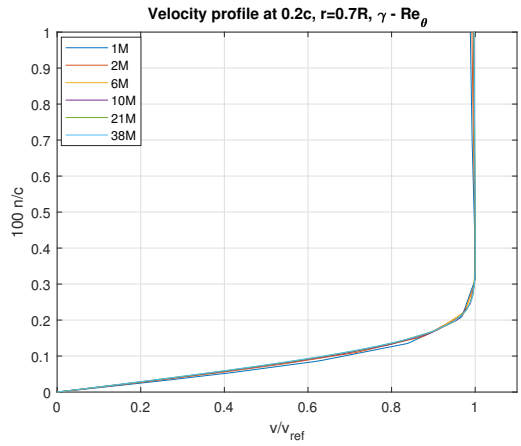

(a) Velocity profile at $x/c = 0.2$.

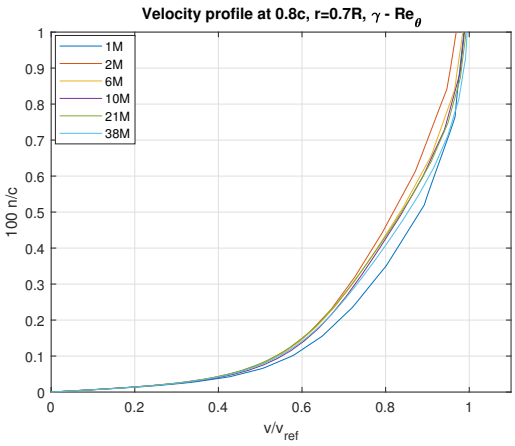

(b) Velocity profile at $x/c = 0.8$.

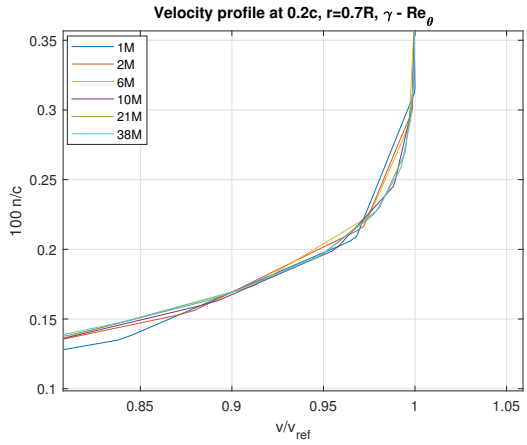

(c) Velocity profile at $x/c = 0.2$.

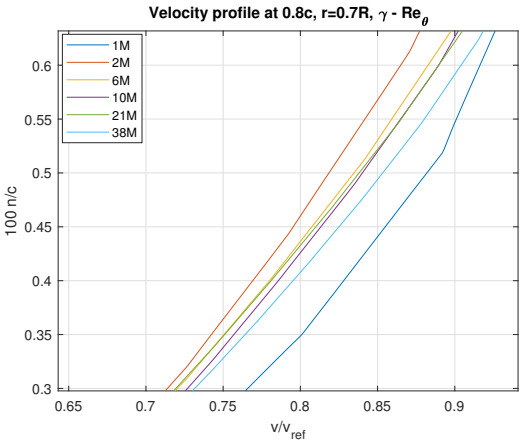

(d) Velocity profile at $x/c = 0.8$.

Figure 5.8: Velocity profile at two points of the chord, located at the radius $r = 0.7R$, for the model $\gamma - \tilde{R}e_{\theta_t}$.

grid size h_i.

Lastly, the estimation of the unknown parameters in equation (5.6) requires a minimum of three grids to be done. The problem, in this case, is that only three grids will not give a reliable result of any of these variables; to counter this, at least four grids are necessary, assuming they are not coarse enough to spoil the estimates. In this Thesis, six grids were used. With this in mind, the determination of the unknowns is done with the least-squares error estimation procedure.

5.3.3 Uncertainty estimation

Estimating the discretization error is important, but the real goal of the Verification process is to determine the uncertainty U_ϕ of the solution, which is an interval that contains the exact solution of the simulation with a 95% confidence:

$$\phi_i - U_\phi \leq \phi_{\text{exact}} \leq \phi_i + U_\phi. \tag{5.8}$$

With the estimation of the uncertainty, the Verification process is concluded and the data can be evaluated accordingly to the procedures proposed by Eça and Hoekstra [41].

5.3.4 Results

After having applied the procedures explained in the previous section, the results were obtained. In Figure 5.9 the results are shown for the thrust coefficient K_T and the torque coefficient K_Q. The independent variable chosen for the representation of these graphics is the refinement ratio h_1/h_i, i.e. the ratio between the typical cell length for the finest grid (grid 38M) versus the typical cell lengths for the other five grids studied. This means that the further right the data point is, the coarser the grid is. In the graphics, the squares and circles represent the values of the results for each grid, and the error bar on the value for the finest grid represents the uncertainty interval on the specific value. Lastly, the lines represented are the fit lines obtained in the uncertainty process and represented by equation (5.6). On the graphic legend, the order of the fit is shown.

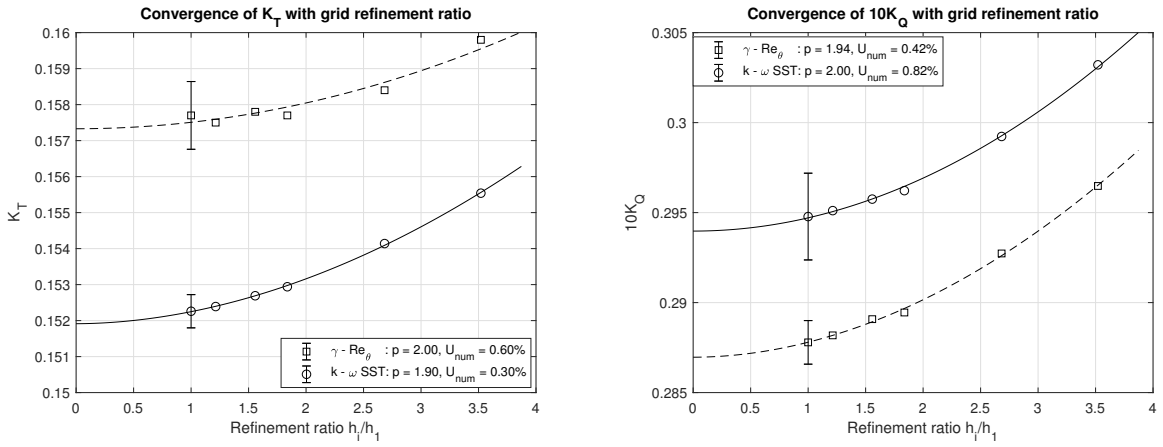

(a) Uncertainty and error estimations for the thrust coefficient K_T.

(b) Uncertainty and error estimations for the torque coefficient K_Q.

Figure 5.9: Results of the Uncertainty and error estimations for the thrust coefficient K_T (left) and the torque coefficient K_Q (right), for both models studied.

Figures 5.9a and b show rather good results for the numerical Verification. For the thrust coefficient, the turbulence shows a lower uncertainty compared to the transition model, even though both are lower than 1%, which is an excellent result. Both models also present almost identical orders for the fitting curve ($p = 1.90$ and $p = 2.00$ respectively).

For the torque coefficient, the results are inverted: the transition model has a lower uncertainty compared to that of the turbulence model, but both models' values are still under $U_{\text{num}} = 1\%$. The orders of the fit lines are still around $p = 2.00$, similar to those of the thrust coefficient.

5.4 Conclusions

In this Chapter, the matter of how the numerical results are affected by grid size has been approached. Different parameters and variables have been analysed, both local (in relation to the flow at any given point) and global (in relation to the whole blade). Finally, the uncertainty generated in the numerical results has been calculated.

The residuals generated in the simulations have shown that despite some irregularities found in their behaviour along the iterations, they show a trend to decrease their value when the simulation progresses. This demonstrates that the simulations have been properly set up and that the results are –at least– accurate enough to be trusted; that does not mean, though, that they are correct compared to the experimental data.

Regarding the iterative errors observed, all of the variables observed showed a very quick stagnation behaviour in all cases and locations (where applicable), with the exception of the 38M which always took longer to stagnate to a single value. This is due to the grid being considerably finer than the other grids used in this work.

Besides the use of different grid sizes for the study, the choice of grids leads to uncertainties generated in the simulations. This, together with the discretization error inherent to the grids, has led to the study of both of these parameters to ensure that the error generated is within acceptable values. The result has been positive, since the uncertainties generated do not exceed $U_{\text{num}} = 1\%$ and the observed order of convergence is around $p = 2$ for all cases studied. This are excellent results and, as such, they can be trusted to be true for the models used in this Thesis. What remains to see now is whether the data obtained fits the experimental data from Jessup or not.

Chapter 6

Blade Flow Analysis & Comparison With Experimental Results

In this Chapter, certain aspects of the boundary layer in the simulations will be studied. They will also be compared to the experimental values extracted from Jessup et al [1], only for the finest grid (38M, in Table 4.2) and both turbulence models. For the $\gamma - \tilde{Re}_{\theta_t}$ model, three different results are considered, with three different turbulent intensities: $Tu = 1.2\%,\ Tu = 1.5\%$, and $Tu = 1.7\%$. The default number of Reynolds for all the results is $Re = 0.73 \times 10^5$ unless otherwise specified.

6.1 Pressure coefficient

The pressure coefficient gives an indication of the pressure distribution along the chord's length. Figure 6.1 below shows the distributions of C_p along the chord for a set radius of $r = 0.7R$. Note that the representation made is of the $-C_p$ so that the line on top represents the suction side of the blade and the lower line represents the pressure side of the blade.

The two models with the results of the finest mesh (38M) are compared in Figure 6.1. From the Figure, it is very clear that both models (and all variations within the $\gamma - \tilde{Re}_{\theta_t}$ model) behave in the same way in predicting the pressure distribution at the blade surface, with minimal differences. The results also show the same trend as the experimental data from Jessup.

For the suction side, the suction peak at around $x/c = 0.3$ is smaller and less steep in the experimental data as is in the obtained results. The differences between the simulated data and the experimental data are relatively small until approximately $x/c = 0.75$, where there is a big change of slope and both sets of data behave in very similar ways.

On the other hand, the pressure side shows a bit more behaviour variation after the suction peak at around $x/c = 0.4$. While the experimental data shows a slow increase in the pressure (remembering

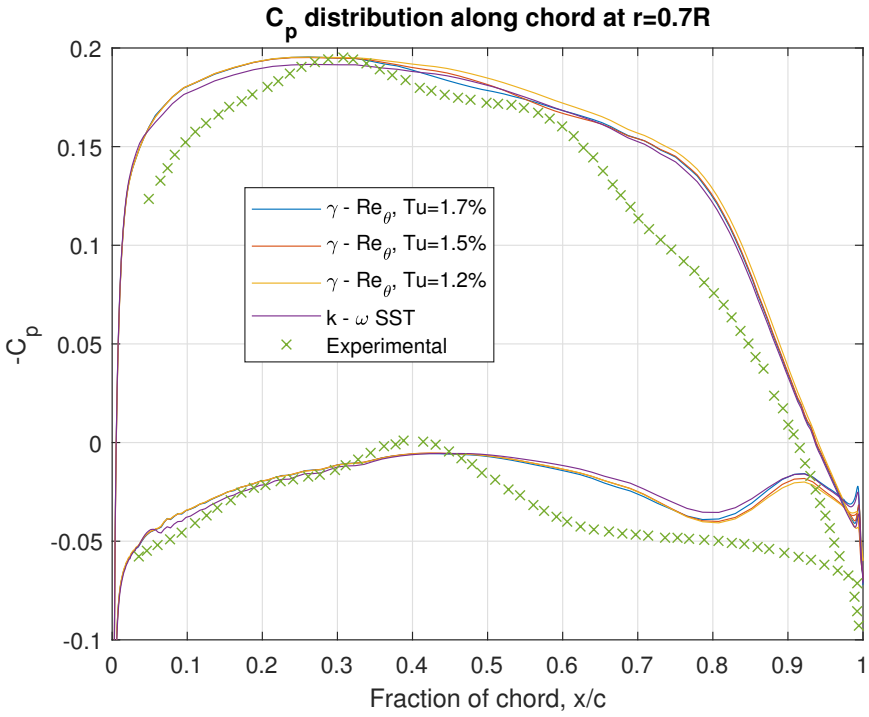

Figure 6.1: Distribution of the pressure coefficient along the chord at $r = 0.7R$ for the two studied models.

that the data shown is the $-C_p$) which maintains the same trend until the end of the chord, the simulated data shows a second suction peak at the very end of the cord, $x/c = 0.9$, which suggests that there is either an unexpected behaviour of the models which is not accounted for, or that there really is a second peak that the original investigation did not detect.

6.2 Velocity profiles

Velocity profiles along the chord wise direction at the 70% of the blade radius show how the boundary layer is modified the more the flow advances towards the trailing edge of the blade. As a consequence to this, the transition area –from laminar to turbulent flow– can be found by simply identifying the region of the chord in which the profiles change noticeably. In the case of the transition model, observing the velocity profiles can be a way of determining whether the turbulence intensity parameter is chosen correctly or not, given that it affects the way in which the flow evolves along the blade. Figures 6.2 and 6.3 below show the velocity profiles along the chord for the cases studied.

The four cases depicted in Figures 6.2 and 6.3 show four degrees of agreement with the experimental data. The first case, corresponding to the data obtained with the $k - \omega$ SST model (Fig. 6.2a), has a quite good agreement with the experimental data from $x/c = 0.6$ onward, suggesting that the transition occurs between $x/c = 0.5$ and 0.6. Prior to that, the adjustment to the experimental data is rather poor, as the profiles –except the first one, which exhibits laminar behaviour– correspond to a turbulent profile, as is expected with this model.

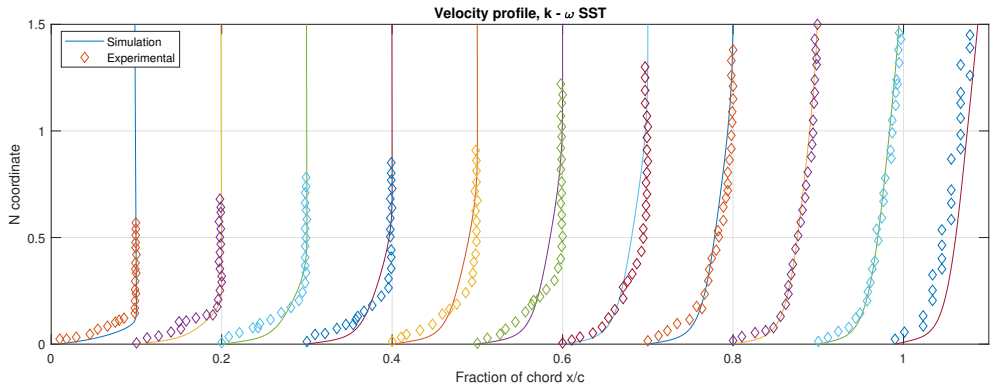

(a) Velocity profiles at $r = 0.7R$ for the $k - \omega$ model.

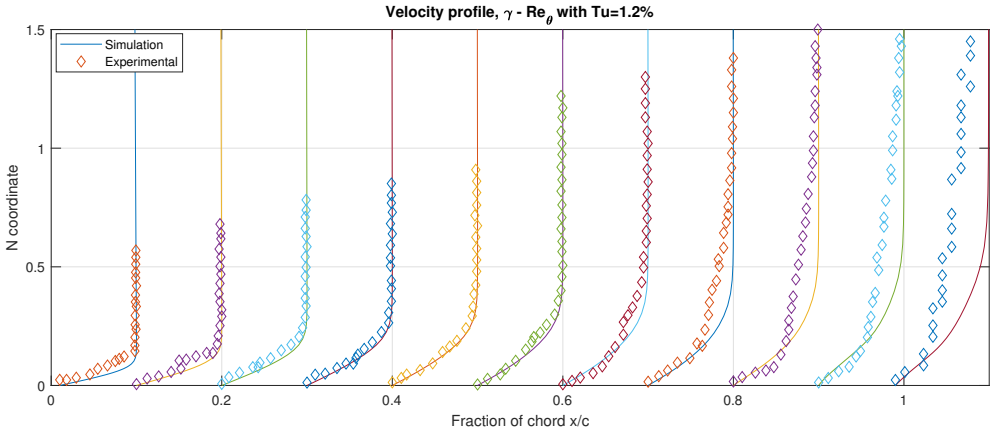

(b) Velocity profiles at $r = 0.7R$ for the $\gamma - \tilde{Re}_{\theta_t}$ model and with $Tu = 1.2\%$.

Figure 6.2: Velocity profiles along the chord at $r = 0.7R$ for the $k-\omega$ SST model and the $\gamma - \tilde{Re}_{\theta_t}$ model, case $Tu = 1.2\%$.

The second case (Figure 6.2b), corresponding to the simulation with the $\gamma - \tilde{Re}_{\theta_t}$ model with $Tu = 1.2\%$, demonstrates a much better agreement with the experimental data for the laminar region of the chord, but not as much on the turbulent region. There is clearly a transition from laminar to turbulent flow, starting at around $x/c = 0.7$, but the evolution of the transition profiles is slow, and does not reach a fully developed turbulent profile before reaching the end of the chord. As a result, the data mismatch between simulation and experimental increases with the fraction of chord.

The third case (Figure 6.3a), for the $\gamma - \tilde{Re}_{\theta_t}$ model with $Tu = 1.5\%$, is the one that agrees the most with the experimental data out of the three cases shown here. The laminar flow is as well-adjusted as is the transition starting at $x/c = 0.6$. The following profiles exhibit practically the same evolution to that of the experimental data. For the rest, it is the best fit so far with the experimental data for this part of the results.

The last case shown (Figure 6.3b), which corresponds to the $\gamma - \tilde{Re}_{\theta_t}$ model with $Tu = 1.7\%$, is very similar to the previous one. There are minor differences at $x/c = 0.5$, where the turbulent profile is a bit more developed in this case, indicating that transition occurs closer to the leading edge of the blade

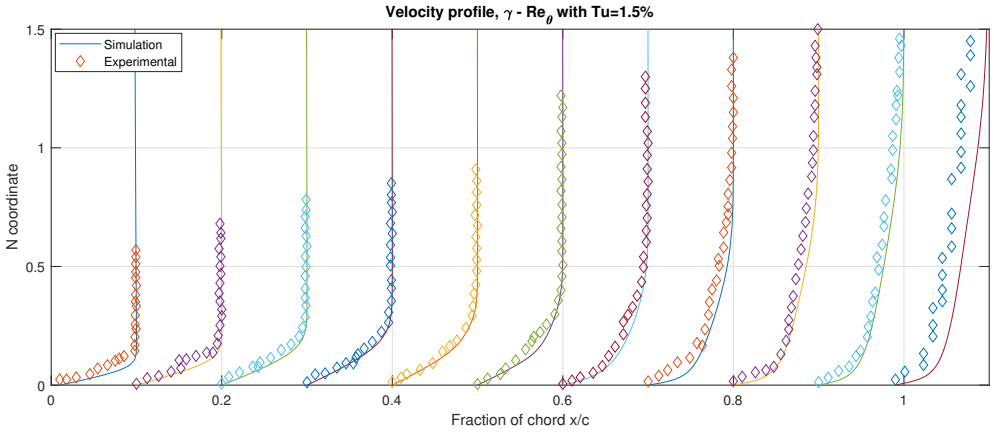

(a) Velocity profiles at $r = 0.7R$ for the $\gamma - \tilde{Re}_{\theta_t}$ model and with $Tu = 1.5\%$.

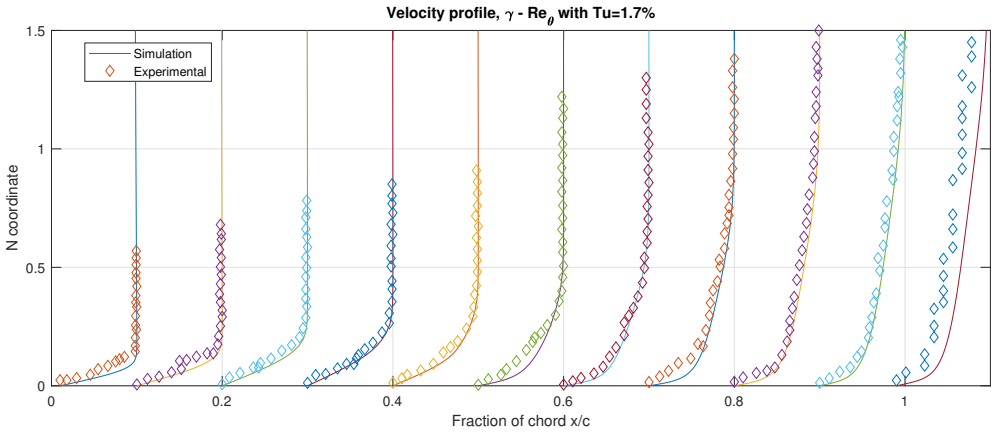

(b) Velocity profiles at $r = 0.7R$ for the $\gamma - \tilde{Re}_{\theta_t}$ model and with $Tu = 1.7\%$.

Figure 6.3: Velocity profiles along the chord at $r = 0.7R$ for the $\gamma - \tilde{Re}_{\theta_t}$ model, cases $Tu = 1.5\%$ and $Tu = 1.7\%$.

compared to the previous case. This result is expected, since a bigger turbulence intensity means an earlier development of the turbulent boundary layer. On the turbulent part of the chord, the data from this case is identical to the one with $Tu = 1.5\%$. The one thing that still does not fit the experimental data is the velocity profile at $x/c = 0.99$, which is the last one depicted in the Figures. Neither this case or the previous one manage to correctly predict the data obtained by Jessup et al.

Overall, it is clear that the case for the transition model with $Tu = 1.5\%$ and $Tu = 1.7\%$ are the ones that adjust best to the experimental data. Despite that, there is not one single case that correctly adjusts the velocity profile to the last profile depicted in Figure 6.2. The aforementioned profile corresponds to the location $x/c = 0.99$. The reason for the data mismatch can be both because of the data available for that profile is not accurate or because the models fail to correctly predict the flow at that point.

6.3 Displacement thickness

The displacement thickness δ^* is a local parameter used in Boundary Layer Theory to measure and study the boundary layer of a certain body. For a two-dimensional boundary layer, such as the one

being analysed in this section, it is defined [29] as

$$\delta^* = \int_0^{\delta} \left(1 - \frac{u(y)}{u_\infty}\right) \mathrm{d}y \tag{6.1}$$

where, similarly to Equation (3.36), u_∞ is the free stream velocity, $u(y)$ is the local velocity and δ is the boundary layer thickness. This last parameter is obtained from the total pressure loss Δp_t in the rotating frame of reference, and is calculated as $\Delta p_t = P + 1/2\rho\,[V_i^2 + V_j^2 + V_k^2] - P_{\text{inlet}} - 1/2\rho\,[v_a^2 + (\Omega 0.7R)^2]$ [34]. The displacement thickness can be interpreted as the distance that the free stream velocity streamline is shifted upwards due to the appearance of the boundary layer. Since the boundary layer thickness increases along the chord-wise direction of the blade, it is to be expected that the results shown will be monotonously increasing, and that on the turbulent region the displacement thickness becomes dramatically bigger still. The results, depicted in Figure 6.4 below, are shown only for the finest mesh (38M) and with the experimental data available. In the same way as the velocity profiles, the variables are plotted adjusted to the normal coordinate to the wall divided by the chord.

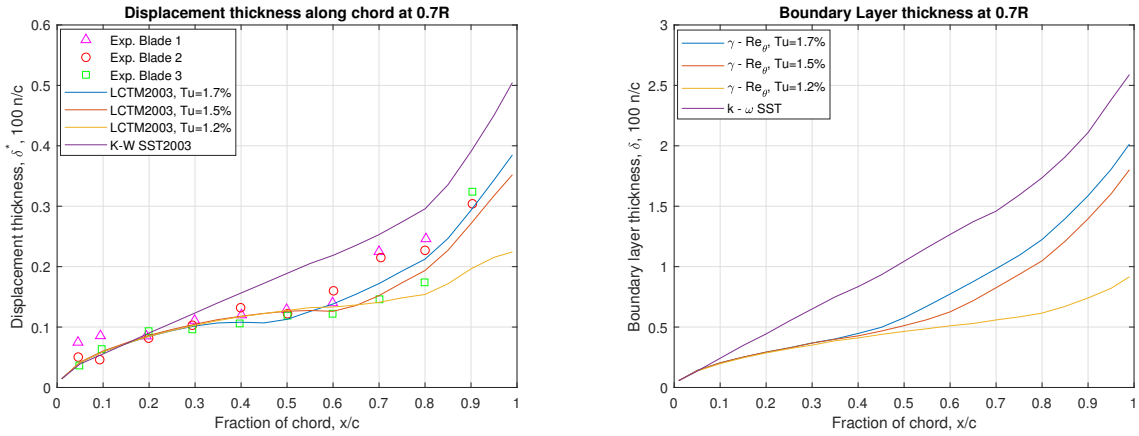

(a) The boundary layer displacement thickness and the experimental data from the literature for both models studied.

(b) The boundary layer thickness along the chord for all cases studied.

Figure 6.4: The boundary layer thickness and displacement thickness for all cases studied, and with experimental data where available.

Generally, the four cases shown exhibit the behaviour described in the previous paragraph, and all results follow a very similar shape as the boundary layer thickness. It can be observed that the tendency of the $k-\omega$ SST model is to overestimate the displacement thickness. Since a turbulent boundary layer is thicker than a laminar one, this result is to be expected. On the other hand, the $\gamma - \tilde{Re}_{\theta_t}$ model has a closer agreement with the experimental data on the laminar part of the flow, but underestimates the values at the turbulent region. This is exacerbated for the case with $Tu = 1.2\%$. This last case is easily explained, since a lower turbulence intensity means, firstly, that the transition region is taken backwards at the blade in the streamwise direction, and then that the turbulent boundary layer will take longer to develop and grow– which in its turn has a direct impact on the displacement thickness. The cases with $Tu = 1.5\%$ and $Tu = 1.7\%$ behave the most similar to each other and also the experimental data. Which is the case that is the most adjusted to the experimental data is not straightforward, since there is some

disparity to this data that the simulated data is being compared to.

6.4 Shape factor

The shape factor, H, is the last parameter of the boundary layer to be studied in this Chapter. It is, by definition, the ratio of the displacement thickness δ^* and the momentum thickness θ, defined in equation (3.36). It is used to measure the type of boundary layer at a certain point on the blade– that is, whether it is laminar or turbulent. For a laminar, two-dimensional boundary layer, also called the Blasius profile, the typical value is $H \approx 2.6$, and for a two-dimensional turbulent boundary layer, the value is $H \approx 1.3$ [29]. Physically, it can be interpreted as how ”fast” the velocity profile at a certain point of the blade reaches the $0.99u_\infty$, which is defined to be the end of the boundary layer. For a laminar flow this happens quicker (in the direction perpendicular to the wall) than for a turbulent flow, and hence why the associated value is higher. For reference, see Figure 6.2; and in Figure 6.5 below the shape factors for the different cases studied are shown.

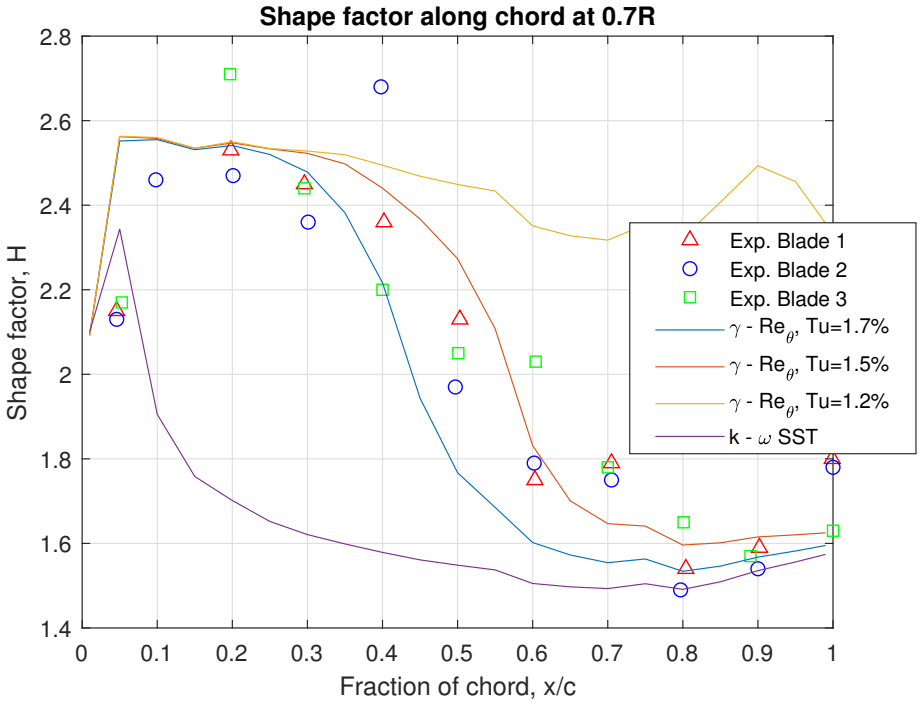

Figure 6.5: The boundary layer shape factor and the experimental data from the literature for both models studied.

The results obtained here are vastly different from one another. To start with, the case with the $k-\omega$ model does not agree at all with the experimental data given in the literature. The explanation is straightforward: since the flow is always turbulent, even though the peak at $x/c \approx 0.05$ suggests the existence of a tiny laminar zone near the leading edge. The rest of the flow is clearly turbulent, hence the shape of the curve and its values generally around $H = 1.5, 1.6$.

The case with the $\gamma - \tilde{Re}_{\theta_t}$ model with $Tu = 1.7\%$ does look a lot better in terms of agreement with the data. The results are coherent with the data, showing both a laminar region with values matching with those proposed by Blasius and a turbulent region with values similar to those related to it. In-between those regions there is a wide transition region, but the slope is the maximum between $x/c = 0.4$ and $x/c = 0.5$; this represents the maximum change in the shape factor, which in turn means the fastest change in the velocity profile: the boundary layer transition region.

The third case, $\gamma - \tilde{Re}_{\theta_t}$ with $Tu = 1.5\%$, has a very similar but delayed behaviour compared to that of the $Tu = 1.7\%$ one. As with the previous parameters studied, the behaviour is delayed a short distance, due to the difference in turbulence intensity, which makes the turbulent boundary layer to develop a bit more slowly compared to the case with higher turbulence intensity. The result is very similar to the previous case commented, since it has a good fit to the experimental data. In this case, the region where the boundary layer transitions here is between $x/c = 0.5$ and $x/c = 0.6$.

The last case shown, with the $\gamma - \tilde{Re}_{\theta_t}$ model and $Tu = 1.2\%$ shows an different behaviour for the model. It starts the same way that the graphic with $Tu = 1.5\%$ does, and the expected result would be to see a decrease in the shape factor value, slower than the previous case but a decrease nonetheless, signalling the transition from turbulent flow. Instead, the shape factor value stagnates around the value $H = 2.4$, which indicates that the flow stays laminar throughout the longitude of the chord. This is a coherent result taking into account what has been shown in previous sections. For instance, the velocity profiles shown in Figure 6.2b shows that there is not a clear transition from laminar to turbulent flow, thus indicating that no such behaviour is to be expected in other parameters that also represent the boundary layer transition. One of these variables is the Friction Coefficient, that shows an important increase in value when the flow changes from laminar to turbulent regime.

6.5 Friction coefficient

The Friction Coefficient, or C_f, is a non-dimensional parameter that measures the value of the shear stress at the wall of the blade compared to that of the free stream dynamic pressure. It is thus defined as

$$C_f = \frac{\tau}{1/2\rho v_a^2} \tag{6.2}$$

where τ is the shear stress at the wall. As previously said, the C_f, besides providing information on the drag originated by the blades, is also used to measure the transition in the boundary layer. This can be done because the friction coefficient increases greatly when the boundary layer enters the turbulent regime. Unfortunately, no experimental data is available for the friction coefficient; despite that, it has been plotted in Figure 6.6 below for the four cases studied.

From Figure 6.6, it is clear that the case of the $\gamma - \tilde{Re}_{\theta_t}$ model, $Tu = 1.7\%$ experiments the transition at around $x/c = 0.5$, as analysed in previous sections. The same goes for the $\gamma - \tilde{Re}_{\theta_t}$ model with

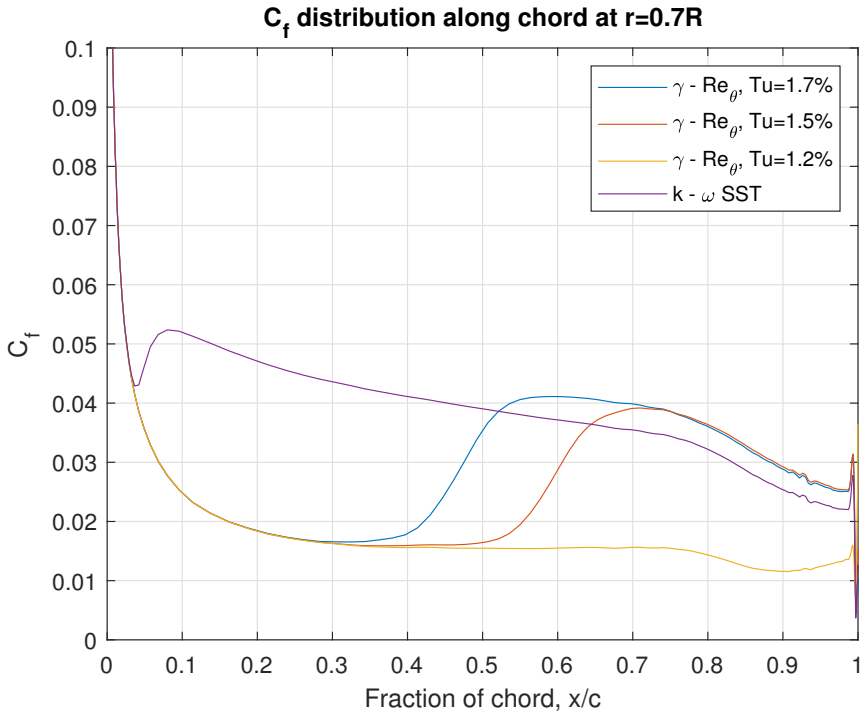

Figure 6.6: Friction coefficient for both models studied.

$Tu = 1.5\%$, which sees the transition delayed a small distance to about $x/c = 0.6$. The $k-\omega$ SST model shows this same behaviour at the very beginning of the blade. This would mean that there is effectively a small region on the blade, near the leading edge, in which the flow could be considered to be laminar; this behaviour was already observed in the previous section, Figure 6.5. It is still less than 5% of the total length of the chord in that particular section of the blade, so it should not be considered significant. Lastly, the $\gamma - \tilde{Re}_{\theta_t}$ model case with $Tu = 1.2\%$ does not show a clear transition point as the other cases do, proving that effectively the shape factor graphic for this case (Figure 6.5) is correct and that there is no transition in that section of the blade for that case.

In the following section a qualitative analysis of the streamlines on the blades will be made, and it will be possible to observe how the streamlines also show where the transition begins and which areas of the blade have a turbulent boundary layer and which ones are laminar.

6.6 Streamlines

Since there is no exact data available, a qualitative analysis of the streamlines in one of the blades will be made in this section. In the literature, Jessup et al study the streamlines in one of the blades of the propeller for the two Reynolds numbers as shown in Table 4.3. Images of the streamlines obtained experimentally using oil dot technique for the same cases have been obtained for the two models studied, and are shown below. The red line indicates the approximate region of transition for the images from the literature.

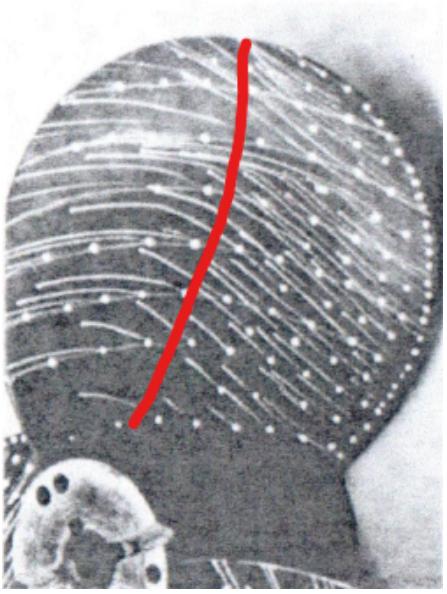

(a) Streamlines from the literature, $Re = 7.3 \times 10^5$, pressure side.

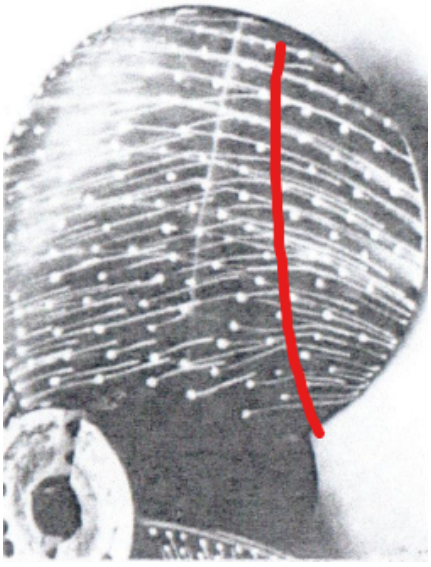

(b) Streamlines from the literature, $Re = 7.3 \times 10^5$, suction side.

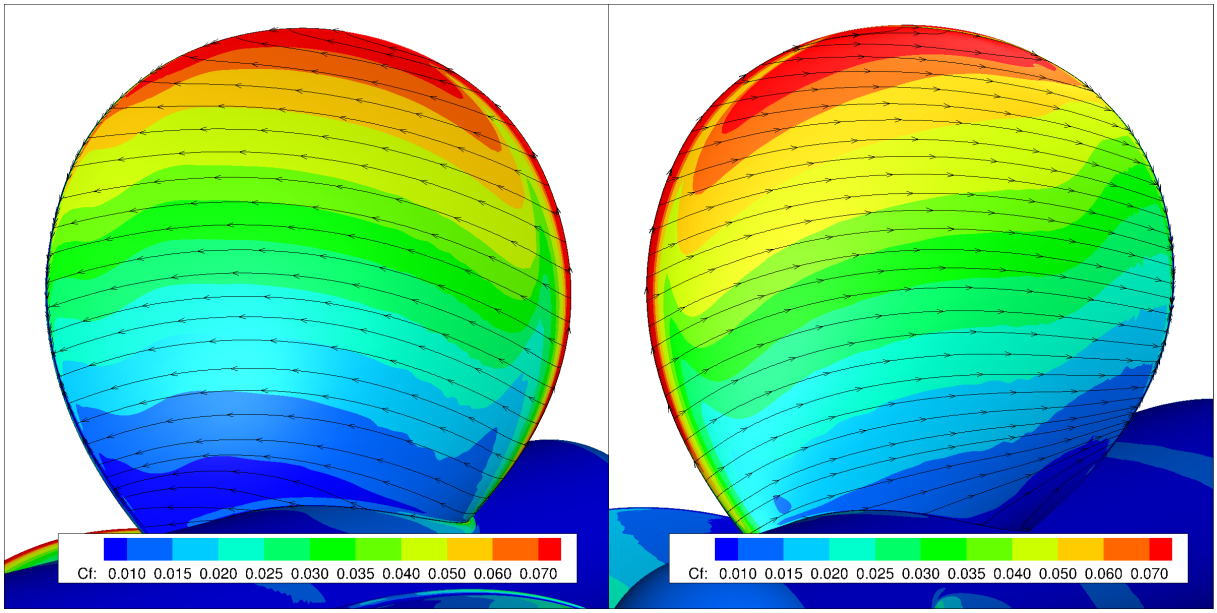

(c) Streamlines obtained from the simulations, $Re = 7.3 \times 10^5$, for the $k - \omega$ model. Left: pressure side. Right: suction side.

Figure 6.7: Streamlines from both the literature [1] and the simulations for the case $Re = 7.3 \times 10^5$ and the $k - \omega$ SST model.

The first case analysed with the lower Reynolds number, $Re = 7.3 \times 10^5$, is the streamlines for the

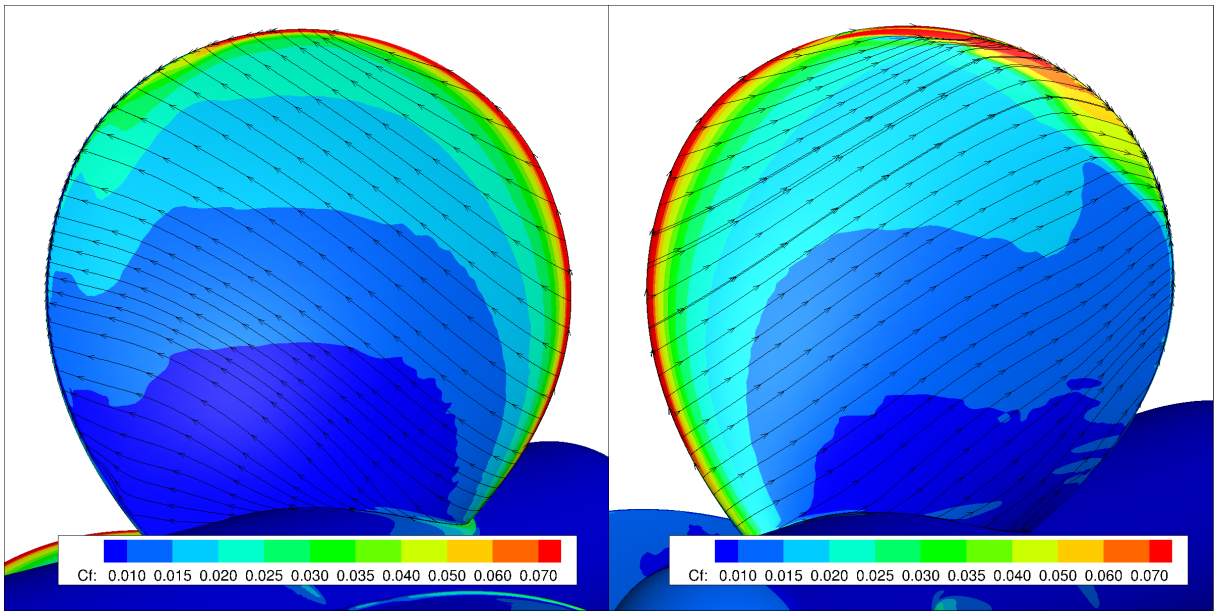

(a) Streamlines obtained from the simulations, $Re = 7.3 \times 10^5$, for the $\gamma - \tilde{Re}_{\theta_t}$ model, with $Tu = 1.2\%$. Left: pressure side. Right: suction side.

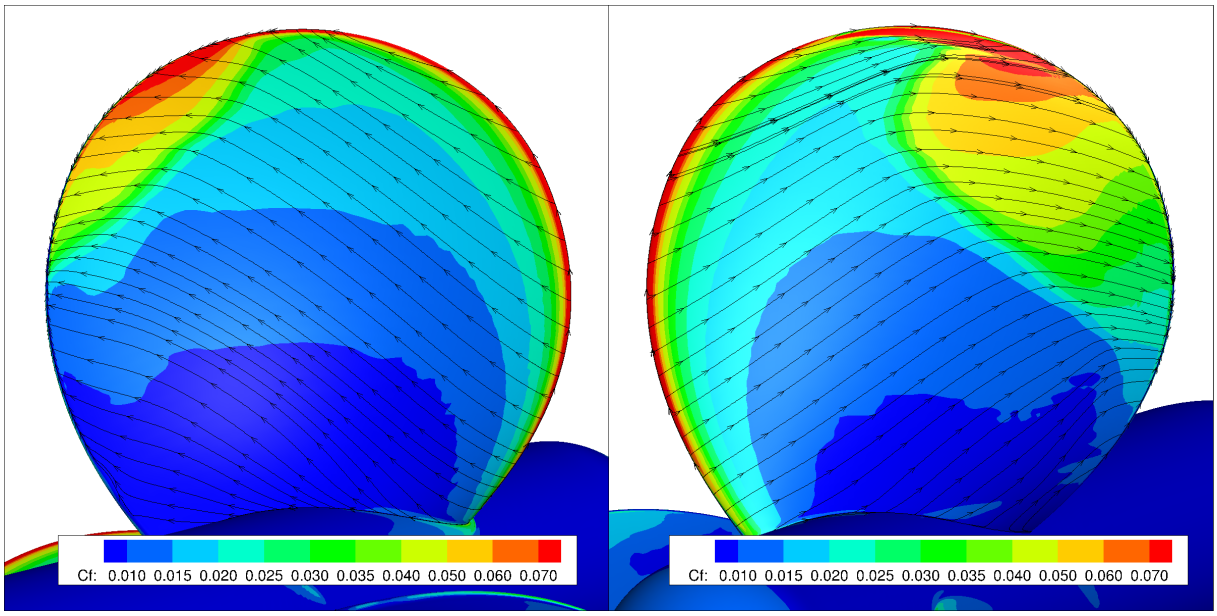

(b) Streamlines obtained from the simulations, $Re = 7.3 \times 10^5$, for the $\gamma - \tilde{Re}_{\theta_t}$ model, with $Tu = 1.5\%$. Left: pressure side. Right: suction side.

Figure 6.8: Streamlines from the simulations for the case $Re = 7.3 \times 10^5$ and the $\gamma - \tilde{Re}_{\theta_t}$ model.

$k - \omega$ SST model, in Figure 6.7c. The results show curved streamlines following only the rotation of the propeller, but do not seem to experiment a change in their direction as they do on Figures 6.7a and b. This means that there is no boundary layer transition on the blade itself: there is only turbulent boundary layer. According to Kuiper [42], a transition in the boundary layer is translated onto the streamlines as a change in their direction, from radius-wise to chord-wise. This happens because of the balance of forces in the different boundary layers: in the laminar boundary layer, the centrifugal forces dominate over the frictional ones, and as such the streamlines approximately follow the radial direction of the blades. On the other hand, in the turbulent boundary layer the centrifugal forces remain constant but the friction

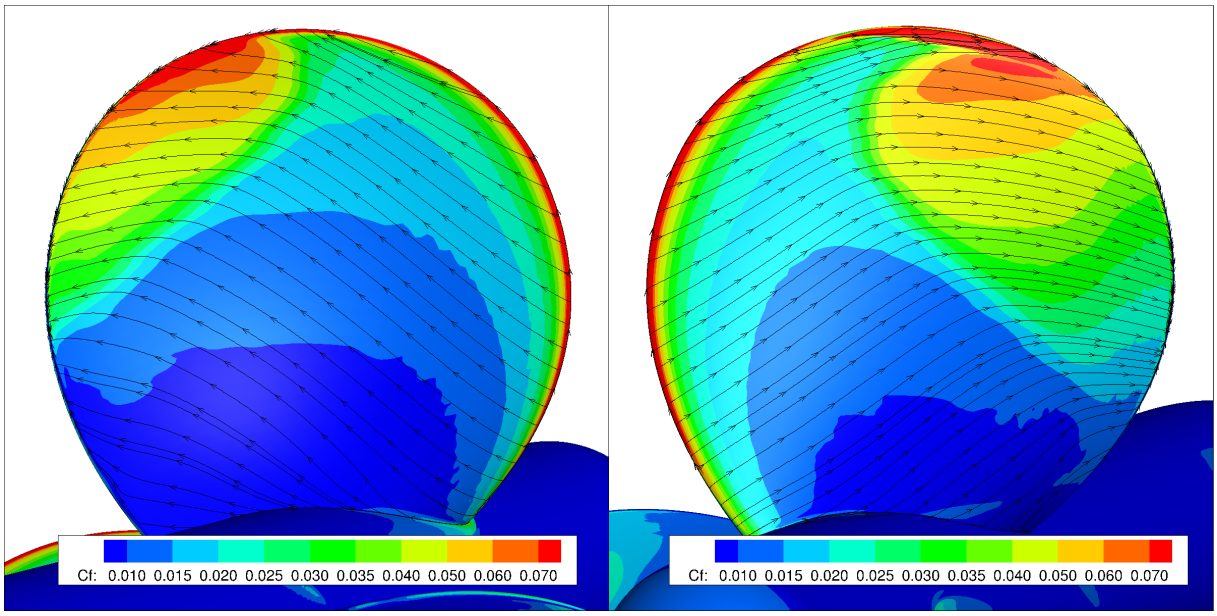

(a) Streamlines obtained from the simulations, $Re = 7.3 \times 10^5$, for the $\gamma - \tilde{Re}_{\theta_t}$ model, with $Tu = 1.7\%$. Left: pressure side. Right: suction side.

Figure 6.9: Streamlines from the simulations for the case $Re = 7.3 \times 10^5$ and the $\gamma - \tilde{Re}_{\theta_t}$ model.

ones increase strongly, imposing a change in the streamlines direction to follow the movement of the blades.

For the $\gamma - \tilde{Re}_{\theta_t}$ model, Figure 6.8, both laminar and turbulent boundary layers can be appreciated at the blade, with the transition region located towards the trailing edge at the very tip of the blade. For the case with $Tu = 1.2\%$ (Figure 6.8a) the transition is not that noticeable, but it is there nevertheless. The case with $Tu = 1.5\%$ shows the most clear transition line and the subsequent change of streamline direction and increase in the friction coefficient. Finally, the case with $Tu = 1.7\%$ show a very similar behaviour to the one with $Tu = 1.5\%$, as it has been shown multiple times. The difference, as seen before, is just a shift in the boundary layer transition regions, while the general streamlines' behaviour is the same.
In Figures 6.10 and 6.11, the results for the case with the higher Reynolds number, $Re = 1.46 \times 10^6$, are shown. Starting with the experimental data, the streamlines from the literature in Figures 6.10a and b show that the higher number of Reynolds produces a smaller change in curvature in the streamlines. It is not an overly exaggerated effect, but it is noticeable nonetheless. For the $k - \omega$ SST model, in Figure 6.10c, the streamlines follow the same pattern as in the previous case with the lower Reynolds number (Figure 6.7c). As commented previously, this is due to the fact that no transition from laminar to turbulent flow exists in this case: all the boundary layer is turbulent.

For the $\gamma - \tilde{Re}_{\theta_t}$ model, in Figure 6.11 (for all Tu values), the effect of increasing the Reynolds number is the advance of the transition region towards the leading edge of the blade. This is especially true for the case for the case with $Tu = 1.7\%$. Compared to the lower Re number, the two regions are distinctly bigger in size, and now the transition effects for the case with $Tu = 1.2\%$ is clearly distinguished in the

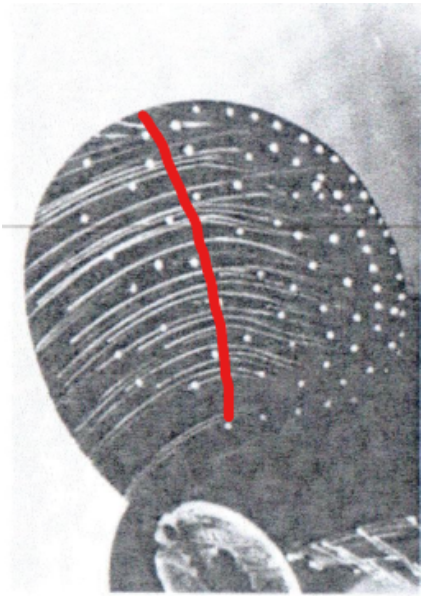

(a) Streamlines from the literature, $Re = 1.46 \times 10^6$, pressure side.

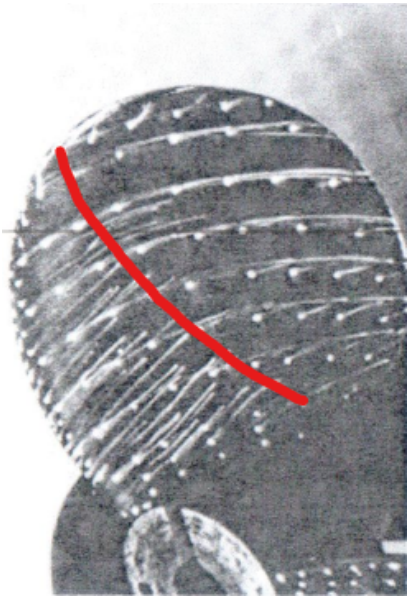

(b) Streamlines from the literature, $Re = 1.46 \times 10^6$, suction side.

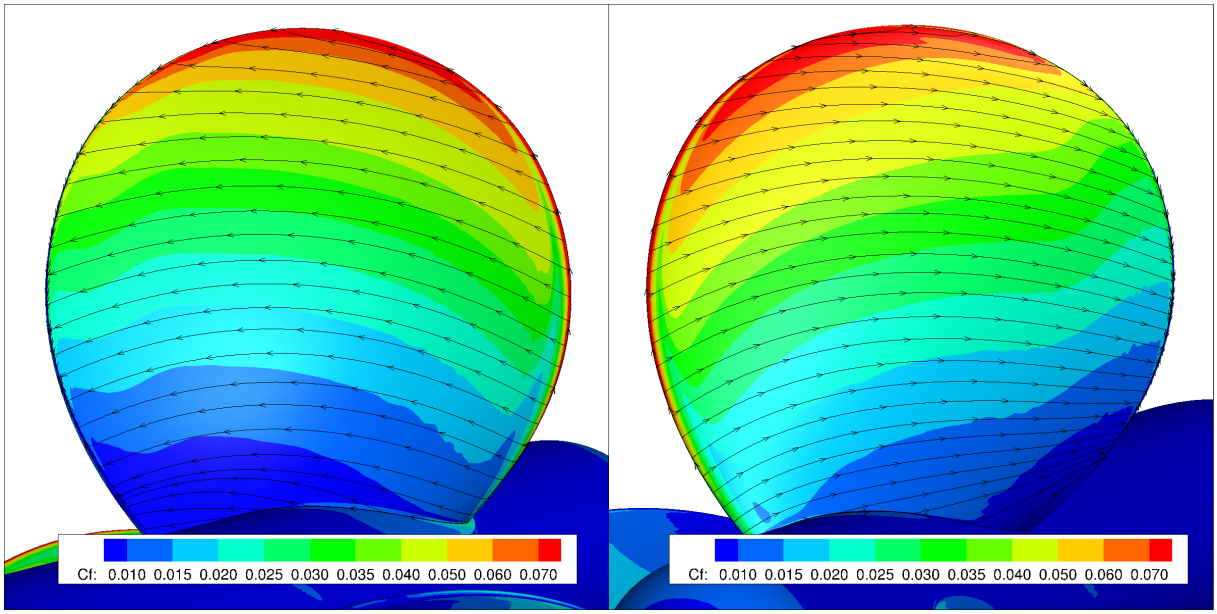

(c) Streamlines obtained from the simulations, $Re = 7.3 \times 10^5$, for the $k - \omega$ model. Left: pressure side. Right: suction side.

Figure 6.10: Streamlines from both the literature [1] and the simulations for the case $Re = 1.46 \times 10^6$ and the $k - \omega$ SST model.

Figure.

Regarding the resemblance to the experimental results, for a higher Re it seems that the case $\gamma - \tilde{Re}_{\theta_t}$ with $Tu = 1.2\%$ has a closer match rather than the case with $Tu = 1.5\%$, but both have a rather similar pattern compared to that depicted in Figures 6.10a and b. The $k - \omega$ SST model, in the same manner as the lower Re, deviates a lot from the experimental data.

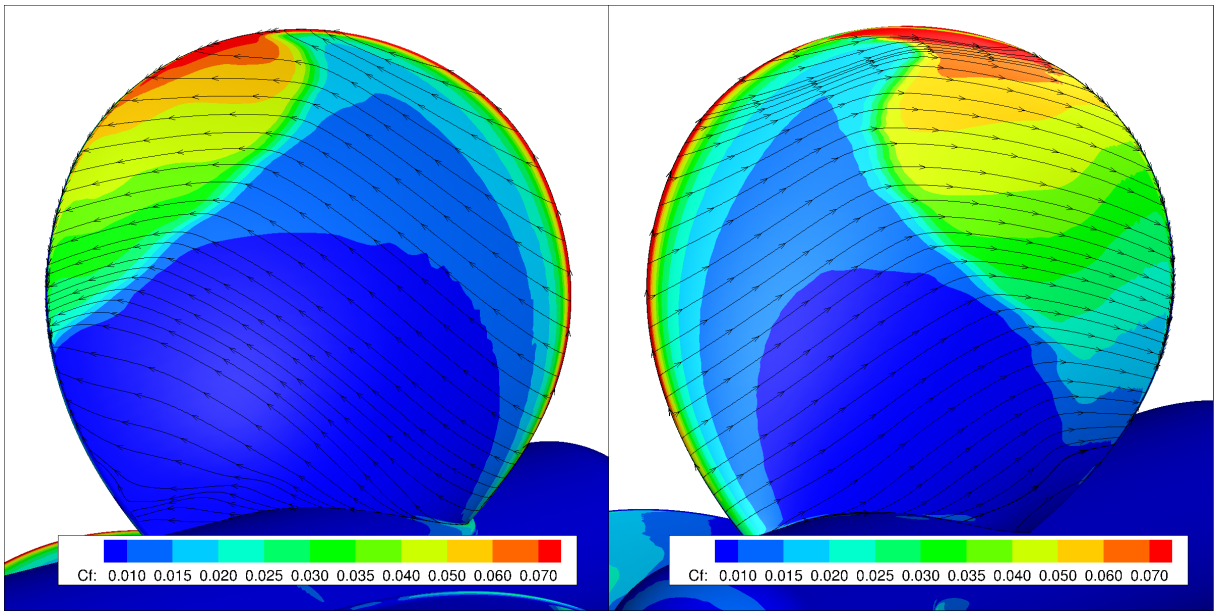

(a) Streamlines obtained from the simulations, $Re = 1.46 \times 10^6$, for the $\gamma - \tilde{Re}_{\theta t}$ model, with $Tu = 1.2\%$. Left: pressure side. Right: suction side.

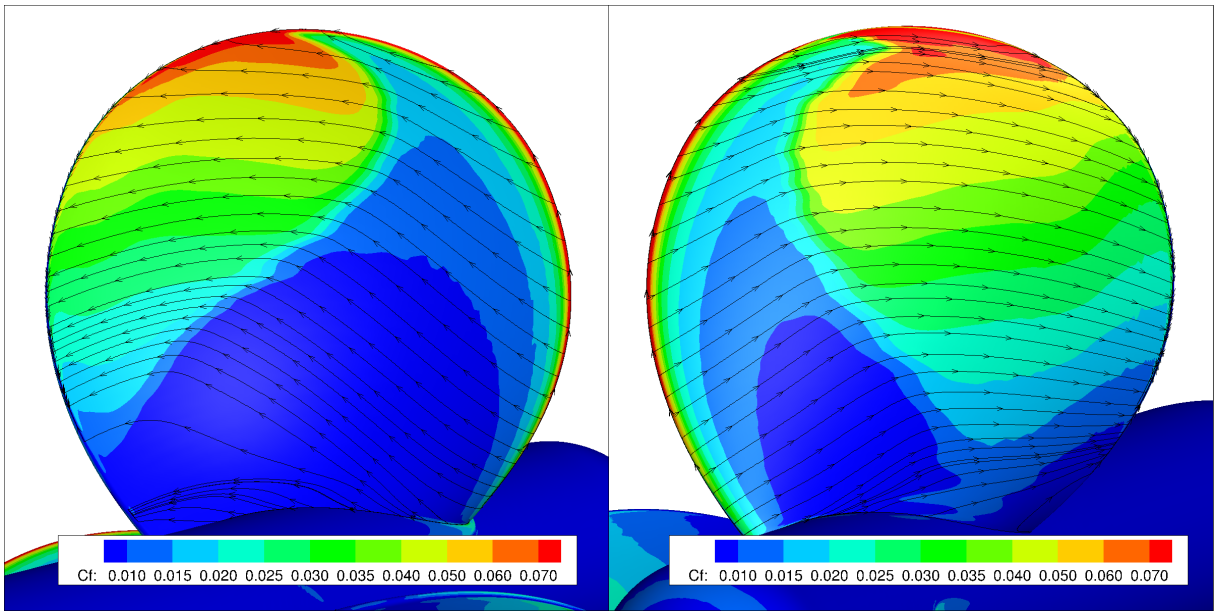

(b) Streamlines obtained from the simulations, $Re = 1.46 \times 10^6$, for the $\gamma - \tilde{Re}_{\theta t}$ model, with $Tu = 1.5\%$. Left: pressure side. Right: suction side.

Figure 6.11: Streamlines from the simulations for the case $Re = 1.46 \times 10^6$ and the $\gamma - \tilde{Re}_{\theta t}$ model.

6.7 Conclusions

In this Chapter, a comparison with the experimental data has been done. Here, the results of simulations with both flow models used, $k - \omega$ SST and $\gamma - \tilde{Re}_{\theta t}$ with its subcases, have been shown. The results obtained have varying degrees of agreement with the experimental data, depending on the variable analysed.

The variable in which all models and subcases have the same level of agreement is the Pressure coefficient. All of the results obtained here behave in the same way, only changing slightly in values, but

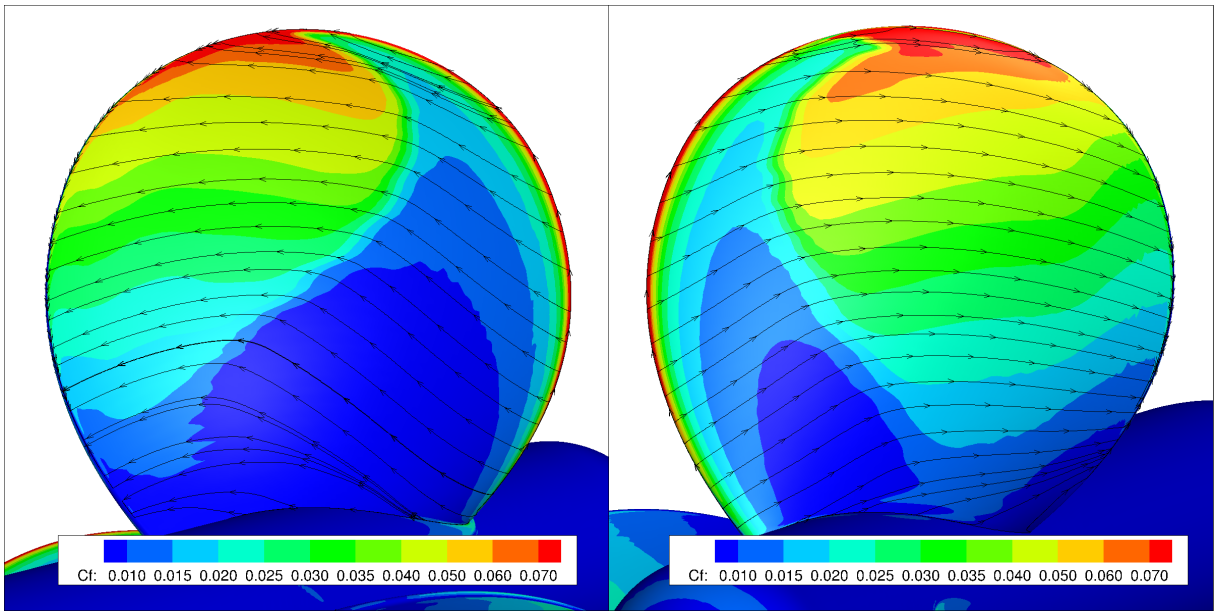

Figure 6.12: Streamlines obtained from the simulations, $Re = 1.46 \times 10^6$, for the $\gamma - \tilde{Re}_{\theta t}$ model, with $Tu = 1.7\%$. Left: pressure side. Right: suction side.

otherwise insignificant. This is noteworthy because no other parameter analysed shows this same level of cohesion between models and subcases. For instance, the velocity profiles along the selected blade chord are vastly different between models. While the $k - \omega$ SST model is a better fit only in the turbulent region of the chord, the $\gamma - \tilde{Re}_{\theta_t}$ model has a better agreement throughout the whole chord.

On the boundary layer parameters (sections 6.3 and 6.4), the $\gamma - \tilde{Re}_{\theta t}$ model presents a clear advantage over the $k - \omega$ SST model. Since the $\gamma - \tilde{Re}_{\theta_t}$ model actually contains a modified $k - \omega$ SST model, as explained in section 3.3.4, Chapter 3, it has the capacity to adapt to both laminar and turbulent regions, given that a proper Tu value is chosen. This is what has been observed in Figures 6.4 and 6.5, in which the $\gamma - \tilde{Re}_{\theta_t}$ model is capable to adapt to the experimental data, while the $k - \omega$ SST is not. On a related note, Figure 6.6, which shows the Friction coefficient along the selected chord, reflects the same data collected in previous sections, despite not having an experimental counterpart, which just furthers the conclusion that in these conditions, the $\gamma - \tilde{Re}_{\theta_t}$ is capable of adapting to the experimental data studied.

The last section studied are the Streamlines on the blades' surface. While the analysis in this aspect is different from other sections (since there is only visual data available), it has still provided the confirmation of all the information extracted from previous parameters: about the ideal use of the $\gamma - \tilde{Re}_{\theta_t}$ model and the *not-so-good* $k - \omega$ SST model. Even in higher Reynolds numbers, the $\gamma - \tilde{Re}_{\theta_t}$ model continues to provide results with better agreement with the experimental data.

Chapter 7

Conclusions

In this Chapter, the general conclusions for the results and the work done in this Thesis will be explained, as well as an analysis of the suitability of the turbulence models used. There will also be a section devoted to proposals of Thesis topics related to the one developed here.

7.1 Results

The simulations performed have yielded the results shown on chapters 5 and 6. These results have demonstrated that the simulations performed have very low numerical uncertainty, present numerical convergence and an observed order of grid convergence of around $p = 2$ for the global variables. This leads to the comparison of the simulated results with the experimental ones: most cases simulated are rather well-adjusted to the data, even if they offer different levels of adjustment.

The different parameters studied were the C_p, the velocity profiles, the displacement thickness, the shape factor and the observed streamlines of the flow. All of these parameters belong to the boundary layer of the flow, and all of them represent in one way or another the evolution of the water flow along the selected chord. In this sense, it has been very interesting to study how these parameters represent the evolution of the boundary layer, as well as how the different models do it.

There are some parameters that present more uniformity than others in the results. For instance, the pressure coefficient gives the most similar results from model to model, with almost no variation whatsoever, followed by the velocity profiles. After this, the displacement thickness and shape factor show less uniformity, with very different results from one case to the other.

7.2 Models used

The first model used, the $k-\omega$ SST model, also referred to as the turbulence model, consists of two equations: one for the kinetic turbulence energy k, eq. (3.16), and another one for the turbulence dissipation ω, eq. (3.17). These two equations regulate how the turbulent flow behaves in the simulations, and the results obtained show as much. The model is limited to that, though– it can only output turbulent flows. This has resulted in a limited agreement of the data given by this model compared to the experimental one, since the flow in this case presents both a laminar region and a turbulent region, with a transition region in between. Nevertheless, in the regions that do fit the experimental data, the model works with a rather good accuracy.

All in all, the model is not the best suited for the use it has been given in this work, given that the turbulent flow is not unique to the case studied.

The second model studied, the $\gamma - \tilde{Re}_{\theta_t}$ model, consists of four equations. One equation is for the flow intermittence γ, the second one is for the transition momentum-thickness Reynolds number $\tilde{Re}_{\theta_t}$. The intermittence regulates the kind of flow that there is, and the $\tilde{Re}_{\theta_t}$ regulates where the transition of the boundary layer occurs. The last two equations are those of the turbulence model, if adapted to fit in with the previous two equations.

This model has demonstrated that it is capable of adapting to different situations. For instance, changing only one parameter –the turbulence intensity– yields distinguishable results that present different behaviours: see, for instance, the difference in the displacement thickness and shape factor shown in Figures 6.4 and 6.5. This trait of the model is what it allows this versatility. To sum up, the $\gamma - \tilde{Re}_{\theta_t}$ model is better suited for the work developed in this Thesis, because of the possible adjustment to the experimental data.

7.3 Objectives

The main objectives of this work were specified in section 1.2. Those objectives included estimating the errors, calculating the flow around the propeller, analyse said flow, and compare the results to the experimental data available.

After reaching this point in the work, the aforementioned objectives can be considered as achieved. The simulations were performed successfully, the comparison with experimental data was done and conclusions were extracted, the errors from the simulations and grid refinement were estimated, the propeller blade flow was analysed including the flow streamlines, and the relevant literature review on the topic was also made.

7.4 Future work

In this section, some proposals are made for the continuation of the work done in this Thesis. These proposals take into account the work done here to either expand it or take it into a new direction. The proposals are as follow:

- Perform the same work done in this Thesis with different turbulence model. One model proposed for this use is the modified Spalart-Allmaras one-equation Transition Model [43, 44], since its simplicity would afford quickness in the calculations and the analysis.
- Recreate the experiment of Jessup et al, to confirm the data obtained and also compared to the simulated data obtained in this work.
- Predict the full-scale performance of propeller P4119 studied in this thesis, with the data obtained by Jessup and the simulated data presented in this Thesis.

Bibliography

[1] S. D. Jessup, C. G. Schott, M. F. Jeffers, and S. Kobayashi. Local Propeller Blade Flows in Uniform and Sheared Onset Flows Using LDV Techniques. In *15th Office of Naval Research Symposium*, pages 221–237, 1984.

[2] A. Moran-Guerrero, J. Gonzalez-Adalid, M. Perez-Sobrino, and L. Gonzalez-Gutierrez. Open Water results comparison for three propellers with transition model, applying crossflow effect, and its comparison with experimental results. In *Fifth International Symposium on Marine Propulsors*, June 2017.

[3] H. Yao and H. Zhang. A simple method for estimating transition locations on blade surface of model propellers to be used for calculating viscous force. *International Journal of Naval Architecture and Ocean Engineering*, 10(4):477–490, 2018. https://doi.org/10.1016/j.ijnaoe.2017.09.002.

[4] X. Wang and K. Walters. Computational Analysis of Marine-Propeller Performance Using Transition-Sensitive Turbulence Modeling. *Journal of Fluids Engineering*, 134:071107, 07 2012. https://doi.org/10.1115/1.4005729.

[5] M. M. Helal, T. M. Ahmed, A. A. Banawan, and M. A. Kotb. Numerical prediction of sheet cavitation on marine propellers using CFD simulation with transition-sensitive turbulence model. *Alexandria Engineering Journal*, 57(4):3805–3815, 2018. ISSN 1110-0168. https://doi.org/10.1016/j.aej.2018.03.008.

[6] M. Staine. The application of 'rans' code to investigate propeller scale effects. In *Defence Evaluation and Research Agency, United Kingdom*, 1998.

[7] V. Krasilnikov, J. Sun, and K. H. Halse. Cfd investigation in scale effect on propellers with different magnitude of skew in turbulent flow. In *First International Symposium on Marine Propulsors*, June 2009.

[8] D. Rijpkema, J. Baltazar, and J. F. de Campos. Viscous flow simulations of propellers in different reynolds number regimes. In *Fourth International Symposium on Marine Propulsors*, June 2015.

[9] A. Bhattacharyya, V. Krasilnikov, and S. Steen. Scale effects on open water characteristics of a controllable pitch propeller working within different duct designs. *Ocean Engineering*, 112:226–242, 2016. https://doi.org/10.1016/j.oceaneng.2015.12.024.

[10] K. W. Shin and P. Andersen. CFD Analysis of Scale Effects on Conventional and Tip-Modified Propellers. In *Fifth International Symposium on Marine Propulsors*, June 2017.

[11] B. Gaurier, C. Carlier, G. Germain, G. Pinon, and E. Rivoalen. Three tidal turbines in interaction: An experimental study of turbulence intensity effects on wakes and turbine performance. *Renewable Energy*, 148:1150–1164, 2020. https://doi.org/10.1016/j.renene.2019.10.006.

[12] M. Togneri, G. Pinon, C. Carlier, C. Choma Bex, and I. Masters. Comparison of synthetic turbulence approaches for blade element momentum theory prediction of tidal turbine performance and loads. *Renewable Energy*, 145:408–418, 2020. https://doi.org/10.1016/j.renene.2019.05.110.

[13] P. A. C. Rocha, H. H. B. Rocha, F. O. M. Carneiro, M. E. V. da Silva, and C. Freitas de Andrade. A case study on the calibration of the $k-\omega$ SST (shear stress transport) turbulence model for small scale wind turbines designed with cambered and symmetrical airfoils. *Energy Journal*, 97:144–150, Dec. 2019. https://doi.org/10.1016/j.energy.2015.12.081.

[14] I. Bouras, L. Ma, D. Ingham, and M. Pourkashanian. An improved k–ω turbulence model for the simulations of the wind turbine wakes in a neutral atmospheric boundary layer flow. *Journal of Wind Eningeering and Industrial Aerodynamics*, 179:358–368, June 2018. https://doi.org/10.1016/j.jweia.2018.06.013.

[15] V. D'Alessandro, S. Montelpare, R. Ricci, and A. Zoppi. Numerical modeling of the flow over wind turbine airfoils by means of Spalart–Allmaras local correlation based transition model. *Energy Journal*, 130:402–409, Apr. 2017. https://doi.org/10.1016/j.energy.2017.04.134.

[16] C. Sicot, P. Devinant, S. Loyer, and J. Hureau. Rotational and turbulence effects on a wind turbine blade. investigation of the stall mechanisms. *Journal of Wind Eningeering and Industrial Aerodynamics*, 96:1320–1331, Apr. 2008. https://doi.org/10.1016/j.jweia.2008.01.013.

[17] A. Rezaeiha, H. Montazeri, and B. Blocken. On the accuracy of turbulence models for CFD simulations of vertical axis wind turbines. *Energy Journal*, 180:838–857, May 2019. https://doi.org/10.1016/j.energy.2019.05.053.

[18] A. Rona, M. El-Dosoky, and D. Adebayo. A hybrid rans model of wing-body junction flow. *European Journal of Mechanics - B/Fluids*, 79:283 – 296, 2020. ISSN 0997-7546. https://doi.org/10.1016/j.euromechflu.2019.09.014.

[19] F. Rizzo, V. D'Alessandro, S. Montelpare, and L. Giammichele. Computational study of a bluff body aerodynamics: Impact of the laminar-to-turbulent transition modelling. *International Journal of Mechanical Sciences*, 178:105620, Mar. 2020. https://doi.org/10.1016/j.ijmecsci.2020.105620.

[20] J. Anderson. *Computational Fluid Dynamics: The Basics With Applications*. McGraw-Hill, 1995.

[21] O. Zienkiewicz, R. Taylor, and P. Nithiarasu. Chapter 8 - turbulent flows. In O. Zienkiewicz, R. Taylor, and P. Nithiarasu, editors, *The Finite Element Method for Fluid Dynamics (Seventh Edition)*, pages

283–308. Butterworth-Heinemann, Oxford, seventh edition edition, 2014. ISBN 978-1-85617-635-4. https://doi.org/10.1016/B978-1-85617-635-4.00008-X.

[22] J. H. Ferziger and M. Peric. *Computational Methods for Fluid Dynamics*. Springer-Verlag Berlin Heidelberg, 1997.

[23] J. Baltazar, D. Rijpkema, and J. Falcão de Campos. On the use of the gamma - re theta transition model for the prediction of the propeller performance at model-scale. *Ocean Engineering*, 170: 6–19, 2018. ISSN 0029-8018. https://doi.org/10.1016/j.oceaneng.2018.10.005.

[24] J. Tyldesley. *An introduction to Tensor Analysis: For Engineers and Applied Scientists*. Longman, 1973.

[25] F. R. Menter. Two-equation eddy-viscosity turbulence models for engineering applications. *American Institute of Aeronautics and Astronautics Journal*, 32:1598–1605, 1994. https://doi.org/10.2514/3.12149".

[26] F. Menter, M. Kuntz, and R. Langtry. Ten Years of Industrial Experience with the SST Turbulence Model. In Begell House Inc, editor, *4th International Symposium on Turbulence, Heat and Mass Transfer*, volume 4, pages 625–632, 2003.

[27] R. B. Langtry and F. R. Menter. Correlation-based transition modeling for unstructured parallelized computational fluid dynamics codes. *American Institute of Aeronautics and Astronautics Journal*, 47:2894–2906, 2009. https://doi.org/10.2514/1.42362.

[28] E. R. Van Driest and C. Blumer. Boundary Layer Transition: Freestream Turbulence and Pressure Gradient Effects. *American Institute of Aeronautics and Astronautics Journal*, 1:1303–1306, 1963. https://doi.org/10.2514/3.1784.

[29] S. B. Pope. *Turbulent Flows*. Cambridge University Press, 2000. https://doi.org/10.1017/CBO9780511840531.

[30] R. B. Langtry. *A Correlation-Based Transition Model using Local Variables for Unstructured Parallelized CFD codes*. PhD thesis, Institut für Thermische Strömungsmaschinen und Maschinenlaboratorium - Universität Stuttgart, May 2006.

[31] *ReFRESCO Theory Manual*. Maritime Research Institute Netherlands, 6700 AA Wagenringen, The Netherlands, 2.4.0 edition, Oct. 2017.

[32] S. B. Denny. *Cavitation and Open-Water performance tests of a series of propellers designed by lifting-surface methods*. Department of the Navy– Naval Ship Research and Development Center, Washington D.C. 20007, Sept. 1968.

[33] J. M. Baltazar, D. R. Rijpkema, and J. A. Falcão de Campos. Numerical studies for verification and validation of open-water propeller rans computations. In *VI International Conference on Computational Methods in Marine Engineering*, 2015.

[34] J. Baltazar, D. Melo, and D. Rijpkema. Analysis of the Blade Boundary-Layer Flow of a Marine Propeller with RANS. In *VIII International Conference on Computational Methods in Marine Engineering*, May 2019.

[35] R. Liebrand. Tip vortex modelling for cavitation noise applications: A verification and validation study in ReFRESCO. Master's thesis, Delft University of Technology, July 2012.

[36] Y. Saad and M. H. Schultz. GMRES: A Generalized Minimal Residual Algorithm for Solving Nonsymmetric Linear Systems. *SIAM Journal on Scientific and Statistical Computing*, 7(3):856–869, 1986. https://doi.org/10.1137/0907058.

[37] M. R. Hestenes and E. Stiefel. Methods of Conjugate Gradients for Solving Linear Systems. *Journal of Research of the National Bureau of Standards*, 49(6):409–436, 1952. https://doi.org/10.6028%2Fjres.049.044.

[38] B. W. Boehm. *Software Engineering Economics*. Prentice-Hall, 1981.

[39] F. G. Blottner. Accurate Navier-Stokes Results for the Hypersonic Flow over a Spherical Nosetip. *Journal of Spacecraft and Rockets*, 27(2):113–122, 1990. https://doi.org/10.2514/3.26115.

[40] L. Eça and M. Hoekstra. Verification and Validation for Marine Applications of CFD. In *20th Symposium on Naval Hydrodynamics*, Aug. 2012.

[41] L. Eça and M. Hoekstra. A procedure for the estimation of the numerical uncertainty of CFD calculations based on grid refinement studies. *Journal of Computational Physics*, 262:104–130, 2014. https://dx.doi.org/10.1016/j.jcp.2014.01.006.

[42] G. Kuiper. *Cavitation inception on ship propeller models*. PhD thesis, Technische Hogeschool Delft, 1981.

[43] S. C. Cakmakcioglu, O. Bas, R. Mura, and U. Kaynak. Ta revised one-equation transitional model for external aerodynamics. In *AIAA Aviation Forum*, 2020. https://doi.org/10.2514/6.2020-2706.

[44] A. Rona, M. El-Dosoky, and D. Adebayo. A revised one-equation transitional model for external aerodynamics. *AIAA Paper*, 79:2020–2076, 2020. https://doi.org/10.2514/6.2020-2706.

Appendix A

ReFRESCO Control file

This appendix contains an exemple of a ReFRESCO control file. The one presented corresponds to the simulation using the $k-\omega$ SST model with the 38M grid.

```
<?xml version="1.0"?>
<controls>
<general>
<codeVersion>2.5</codeVersion>
<name>P4119</name>
<description>P4119 propeller</description>
<caseid>P4119</caseid>
<material>WATER</material>
<referenceLength>0.1409</referenceLength>
<referenceVelocity>5.00058</referenceVelocity>
<referenceMaterial>WATER</referenceMaterial>
<referencePressure>0.0</referencePressure>
<outFileName>P4119</outFileName>
<outFilePath>.</outFilePath>
<nsave>500</nsave>
<suppressOutput>false</suppressOutput>
</general>

<materials>
<material name="WATER">
<fluid>
<viscosityMolecular>9.601e-4</viscosityMolecular>
<density>997.83</density>
<variableDensity>false</variableDensity>
</fluid>
</material>
</materials>

<accelerationOfGravity>
<apply>false</apply>
<gravityVector>0. 0. 9.81</gravityVector>
</accelerationOfGravity>

<grids>
<grid>
<gridFilePath>../../../../Grids</gridFilePath>
<gridFileName>P4119_Grid38MCells</gridFileName>
<subGrids>
<subGrid name="Interior">
```

```
<moveGridApply>true</moveGridApply>
<moveGridMethod>AFM</moveGridMethod>
<moveGridUserDefined>false</moveGridUserDefined>
<calcEqsOfMotion>false</calcEqsOfMotion>
<rotationOrigin>0.0 0.0 0.0</rotationOrigin>
<rotationAxis>1.0 0.0 0.0</rotationAxis>
<rotationRate>43.98229715</rotationRate>
<translationVelocity>0.0 0.0 0.0</translationVelocity>
<initialDispApply>false</initialDispApply>
<initialDispRotationOrigin>0.0 0.0 0.0</initialDispRotationOrigin>
<initialDispRotationAxis>1.0 0.0 0.0</initialDispRotationAxis>
<initialDispRotationAngle>0.0</initialDispRotationAngle>
<initialDispTranslation>0.0 0.0 0.0</initialDispTranslation>
<saveMoveGridExtraQuantities>false</saveMoveGridExtraQuantities>
</subGrid>
</subGrids>
</grid>
</grids>

<boundaries>
<family name="BCFarfield">
<BCPressure>
<pressure>0.0</pressure>
<extrapolationOrder>0</extrapolationOrder>
</BCPressure>
</family>

<family name="BCInflow" >
<BCInflow>
<velocity userCode="false">-1.72081 0 0</velocity>
<checkFlux>true</checkFlux>
<referenceSystem>EARTH_FIXED</referenceSystem>
<extrapolationOrder>0</extrapolationOrder>
<turbulence>
<turbIntensity_eddyVisc>
<turbIntensity userCode="false">1.e-2</turbIntensity>
<eddyVisc userCode="false">1.0</eddyVisc>
</turbIntensity_eddyVisc>
</turbulence>
</BCInflow>
</family>

<family name="BCOutflow">
<BCOutflow>
<extrapolationOrder>0</extrapolationOrder>
</BCOutflow>
</family>

<family name="BCWall">
<BCWall>
<velocity userCode="false">0 0 0</velocity>
<referenceSystem>BODY_FIXED</referenceSystem>
<extrapolationOrder>0</extrapolationOrder>
<useWallFunction>AUTOMATIC</useWallFunction>
</BCWall>
</family>

<family name="BCWallInviscid">
```

```
<BCWall>
<velocity userCode="false">0 0 0</velocity>
<referenceSystem>BODY_FIXED</referenceSystem>
<extrapolationOrder>0</extrapolationOrder>
<useWallFunction>AUTOMATIC</useWallFunction>
</BCWall>
</family>

<family name="BCWallViscous">
<BCWall>
<velocity userCode="false">0 0 0</velocity>
<referenceSystem>BODY_FIXED</referenceSystem>
<extrapolationOrder>0</extrapolationOrder>
<useWallFunction>AUTOMATIC</useWallFunction>
</BCWall>
</family>

<family name="BCWallViscousHeatFlux">
<BCWall>
<velocity userCode="false">0 0 0</velocity>
<referenceSystem>BODY_FIXED</referenceSystem>
<extrapolationOrder>0</extrapolationOrder>
<useWallFunction>AUTOMATIC</useWallFunction>
</BCWall>
</family>
</boundaries>

<bodies />
<coprocessing />

<timeLoop>
<unsteady>false</unsteady>
<solutionScheme>IMPLICIT_EULER</solutionScheme>
<maxTimesteps>100</maxTimesteps>
<timeDelta>0.001</timeDelta>
</timeLoop>

<adaptLoop />

<outerLoop>
<maxIteration>200000</maxIteration>
<convergenceTolerance>1e-6</convergenceTolerance>
<residualNorm>INFINITY</residualNorm>
<divergenceTolerance>1e+9</divergenceTolerance>
</outerLoop>

<restart>
<restart>true</restart>
<useLastTimeStep>false</useLastTimeStep>
<resetCounter>false</resetCounter>
<restartFileName>P4119</restartFileName>
<restartFilePath>.</restartFilePath>
</restart>

<massMomentumSolver>
<solverType name="SEGREGATED">
<segregated>
<solver>FRESCO</solver>
```

```
</segregated>
</solverType>
</massMomentumSolver>

<equations>
<equation name="mom">
<EQMomentum>
<solve_x>true</solve_x>
<solve_y>true</solve_y>
<solve_z>true</solve_z>
<solver>
<PETSC>
<solver>GMRES</solver>
<preconditioner>JACOBI</preconditioner>
</PETSC>
</solver>
<convergenceTolerance>0.01</convergenceTolerance>
<maxIteration>400</maxIteration>
<relaxationProcedure>
<IMPLICIT_EXPLICIT>
<imp_relax_min>0.6</imp_relax_min>
<imp_relax_max>0.6</imp_relax_max>
<imp_relax_fac>5000</imp_relax_fac>
<exp_relax>0.1</exp_relax>
</IMPLICIT_EXPLICIT>
</relaxationProcedure>
<convectiveFluxDiscretisation>
<TVD_SCHEME>
<schemeName>LIMITED_QUICK</schemeName>
</TVD_SCHEME>
<!--FOU_CDS_BLEND>
<blendingFactor>0.0</blendingFactor>
</FOU_CDS_BLEND-->
</convectiveFluxDiscretisation>
<gradientCalculation>
<GAUSS>
</GAUSS>
</gradientCalculation>
<applyEccentricityCorrection>true</applyEccentricityCorrection>
<userSource>false</userSource>
<residualNormalisation>PARNASSOS_LIKE</residualNormalisation>
<toSave>true</toSave>
<saveResidual>true</saveResidual>
<saveChanges>false</saveChanges>
<saveGradients>false</saveGradients>
<saveCourantNo>false</saveCourantNo>
<savePecletNo>false</savePecletNo>
<saveShearStress>true</saveShearStress>
<saveYplus>true</saveYplus>
<initialization>
<FAMILY_BASED>
<familyName>BCInflow</familyName>
</FAMILY_BASED>
</initialization>
</EQMomentum>
</equation>

<equation name="pres">
```

```
<EQPressure>
<solver>
<PETSC>
<solver>CG</solver>
<preconditioner>JACOBI</preconditioner>
</PETSC>
</solver>
<convergenceTolerance>0.01</convergenceTolerance>
<maxIteration>400</maxIteration>
<relaxationProcedure>
<EXPLICIT>
<exp_relax>0.15</exp_relax>
</EXPLICIT>
</relaxationProcedure>
<gradientCalculation>
<GAUSS></GAUSS>
</gradientCalculation>
<applyEccentricityCorrection>true</applyEccentricityCorrection>
<userSource>false</userSource>
<residualNormalisation>PARNASSOS_LIKE</residualNormalisation>
<toSave>true</toSave>
<saveResidual>true</saveResidual>
<saveGradients>false</saveGradients>
<saveChanges>false</saveChanges>
<initialPressure userCode="false">0.0</initialPressure>
</EQPressure>
</equation>

<equation name="turb">
<EQTurbulence>
<turbulenceModel>
<K_OMEGA>
<MODELTYPE>SST_2003</MODELTYPE>
</K_OMEGA>
</turbulenceModel>
<solver>
<PETSC>
<solver>GMRES</solver>
<preconditioner>BJACOBI</preconditioner>
</PETSC>
</solver>
<convergenceTolerance>0.1</convergenceTolerance>
<maxIteration>200</maxIteration>
<relaxationProcedure>
<IMPLICIT_EXPLICIT>
<imp_relax_min>0.6</imp_relax_min>
<imp_relax_max>0.6</imp_relax_max>
<imp_relax_fac>5000</imp_relax_fac>
<exp_relax>0.10</exp_relax>
</IMPLICIT_EXPLICIT>
</relaxationProcedure>
<relaxEddyViscosity>0.25</relaxEddyViscosity>
<relaxAnisotropy>0.1</relaxAnisotropy>
<stagnationRegionCorrection>
<REALIZABILITY>
<realizabilityLimiter>10.0</realizabilityLimiter>
</REALIZABILITY>
</stagnationRegionCorrection>
```

```
<convectiveFluxDiscretisation>
<FOU_CDS_BLEND>
<blendingFactor>0.0</blendingFactor>
</FOU_CDS_BLEND>
</convectiveFluxDiscretisation>
<gradientCalculation>
<GAUSS></GAUSS>
</gradientCalculation>
<applyEccentricityCorrection>false</applyEccentricityCorrection>
<toSave>true</toSave>
<toSaveEddyVisc>true</toSaveEddyVisc>
<toSaveTurbulenceIntensity>false</toSaveTurbulenceIntensity>
<toSaveVonKarmanLength>false</toSaveVonKarmanLength>
<toSaveAnisotropy>false</toSaveAnisotropy>
<toSaveSASTerm>false</toSaveSASTerm>
<toSaveCurvatureRotationCorrection>false</toSaveCurvatureRotationCorrection>
<userSource>false</userSource>
<saveResidual>true</saveResidual>
<saveChanges>false</saveChanges>
<saveGradients>false</saveGradients>
<saveEddyViscGradients>false</saveEddyViscGradients>
<residualNormalisation>PARNASSOS_LIKE</residualNormalisation>
<initialization>
<turbIntensity_eddyVisc>
<turbIntensity userCode="false">1.e-2</turbIntensity>
<eddyVisc userCode="false">1.0</eddyVisc>
</turbIntensity_eddyVisc>
</initialization>
</EQTurbulence>
</equation>
</equations>

<extraQuantities>
<saveVorticity>true</saveVorticity>
<saveQCriterion>true</saveQCriterion>
</extraQuantities>

<monitors>
<monitor name="ForcesBlades">
<MO_Force>
<fileName>forces_blades</fileName>
<saveFrequency>1</saveFrequency>
<label></label>
<families>BCWall BCWallInviscid BCWallViscous</families>
<forTecplot>true</forTecplot>
</MO_Force>
</monitor>

<monitor name="ForcesBlade1">
<MO_Force>
<fileName>forces_blade1</fileName>
<saveFrequency>1</saveFrequency>
<label></label>
<families>BCWall</families>
<forTecplot>true</forTecplot>
</MO_Force>
</monitor>
```

```
<!--monitor name="ForcesBlade2">
<MO_Force>
<fileName>forces_blade2</fileName>
<saveFrequency>1</saveFrequency>
<label></label>
<families>BCWallInviscid</families>
<forTecplot>true</forTecplot>
</MO_Force>
</monitor>

<monitor name="ForcesBlade3">
<MO_Force>
<fileName>forces_blade3</fileName>
<saveFrequency>1</saveFrequency>
<label></label>
<families>BCWallViscous</families>
<forTecplot>true</forTecplot>
</MO_Force>
</monitor-->

<monitor name="ForcesShaft">
<MO_Force>
<fileName>forces_shaft</fileName>
<saveFrequency>1</saveFrequency>
<label></label>
<families>BCWallViscousHeatFlux</families>
<forTecplot>true</forTecplot>
</MO_Force>
</monitor>

<monitor name="MomentsBlades">
<MO_Moment>
<fileName>moments_blades</fileName>
<saveFrequency>1</saveFrequency>
<label></label>
<families>BCWall BCWallInviscid BCWallViscous</families>
<referencePoint>0 0 0</referencePoint>
<forTecplot>true</forTecplot>
</MO_Moment>
</monitor>

<monitor name="MomentsBlade1">
<MO_Moment>
<fileName>moments_blade1</fileName>
<saveFrequency>1</saveFrequency>
<label></label>
<families>BCWall</families>
<referencePoint>0 0 0</referencePoint>
<forTecplot>true</forTecplot>
</MO_Moment>
</monitor>

<!--monitor name="MomentsBlade2">
<MO_Moment>
<fileName>moments_blade2</fileName>
<saveFrequency>1</saveFrequency>
<label></label>
<families>BCWallInviscid</families>
```

```
<referencePoint>0 0 0</referencePoint>
<forTecplot>true</forTecplot>
</MO_Moment>
</monitor>

<monitor name="MomentsBlade3">
<MO_Moment>
<fileName>moments_blade3</fileName>
<saveFrequency>1</saveFrequency>
<label></label>
<families>BCWallViscous</families>
<referencePoint>0 0 0</referencePoint>
<forTecplot>true</forTecplot>
</MO_Moment>
</monitor-->

<monitor name="MomentsShaft">
<MO_Moment>
<fileName>moments_shaft</fileName>
<saveFrequency>1</saveFrequency>
<label></label>
<families>BCWallViscousHeatFlux</families>
<referencePoint>0 0 0</referencePoint>
<forTecplot>true</forTecplot>
</MO_Moment>
</monitor>

<monitor name="Yplus">
<MO_Yplus>
<fileName>scalar_yplus</fileName>
<saveFrequency>1</saveFrequency>
<label></label>
<families>BCWall BCWallInviscid BCWallViscous BCWallViscousHeatFlux</families>
<forTecplot>true</forTecplot>
</MO_Yplus>
</monitor>

<monitor name="Point1">
<MO_Point>
<fileName>pressure_s02_r07_ss</fileName>
<saveFrequency>1</saveFrequency>
<label></label>
<fields>Pressure</fields>
<coordinates>0.2318503437135482E-01 -0.3502721184431454E-01 0.1007527147538079E+00</coordinates>
<includeBoundaryData>true</includeBoundaryData>
<forTecplot>true</forTecplot>
<writeInterpolationPoints>false</writeInterpolationPoints>
<referenceSystem>EARTH_FIXED</referenceSystem>
<bodyFixedReferenceFamily></bodyFixedReferenceFamily>
<interpolation>
<LEAST_SQUARES>
<order>2</order>
<cloudPointMultiplier>2</cloudPointMultiplier>
</LEAST_SQUARES>
</interpolation>
</MO_Point>
</monitor>
```

```
<monitor name="Point2">
<MO_Point>
<fileName>pressure_s08_r07_ss</fileName>
<saveFrequency>1</saveFrequency>
<label></label>
<fields>Pressure</fields>
<coordinates>-0.1465576279464696E-01 0.3897064260544012E-01 0.9930589500039511E-01</coordinates>
<includeBoundaryData>true</includeBoundaryData>
<forTecplot>true</forTecplot>
<writeInterpolationPoints>false</writeInterpolationPoints>
<referenceSystem>EARTH_FIXED</referenceSystem>
<bodyFixedReferenceFamily></bodyFixedReferenceFamily>
<interpolation>
<LEAST_SQUARES>
<order>2</order>
<cloudPointMultiplier>2</cloudPointMultiplier>
</LEAST_SQUARES>
</interpolation>
</MO_Point>
</monitor>

<monitor name="Boundary">
<MO_Boundary>
<fileName>shearstress_blade1</fileName>
<saveFrequency>500</saveFrequency>
<label></label>
<families>BCWall</families>
<fields>ShearStress</fields>
<forTecplot>true</forTecplot>
</MO_Boundary>
</monitor>
</monitors>

<deformGrid />
<adaptiveGrid />
<imposedMotion />
<freeMotion />
<fsi />
<acoustics />
<buoyancyBoussinesq />

<bodyForces>
<apply>false</apply>
<userDefined>false</userDefined>
<toSave>false</toSave>
<bodyforceTreatment>EXPLICIT_SOURCE</bodyforceTreatment>
<bodyForce>0.0 0.0 0.0</bodyForce>
</bodyForces>

<developer>
<pwi_approxInvMomMatnoDt>true</pwi_approxInvMomMatnoDt>
</developer>

<userCode>
</userCode>
</controls>
```

Appendix B

Residuals Graphics

This Appendix contains the graphics of the residuals obtained with TecPlot for all the calculations made throughout the duration of this work. This includes the different grids studied as well as the different flow models and different variations within those as well.

B.1 $\mathrm{k}-\omega$ SST calculations

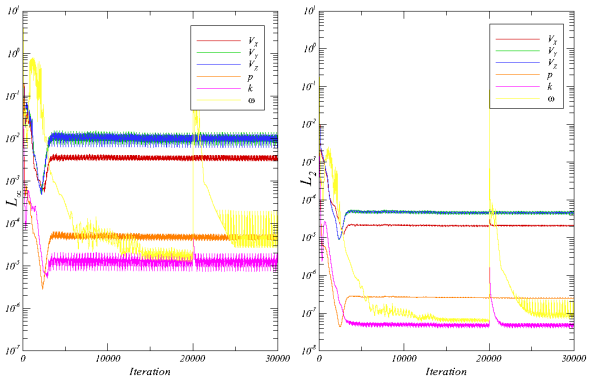

(a) Grid 1M, $k-\omega$ SST Model.

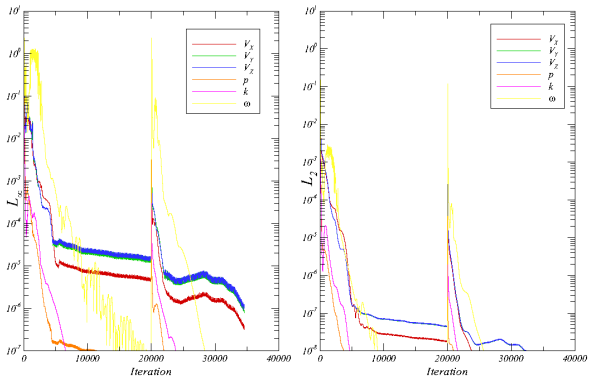

(b) Grid 2M, $k-\omega$ SST Model.

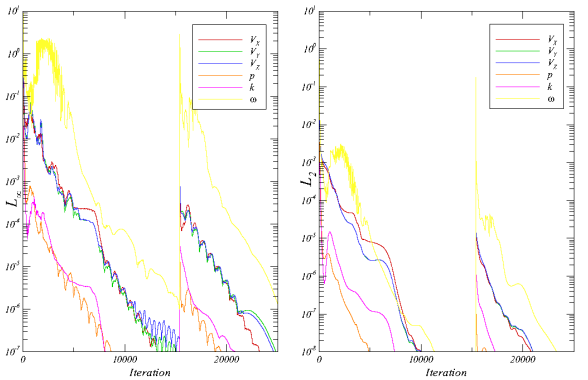

(c) Grid 6M, $k-\omega$ SST Model.

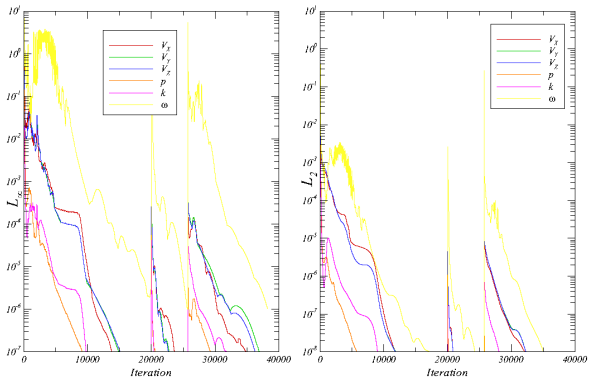

(d) Grid 10M, $k-\omega$ SST Model.

Figure B.1: Residuals graphics for the grids 1M, 2M, 6M, and 10M. $k-\omega$ SST Model.

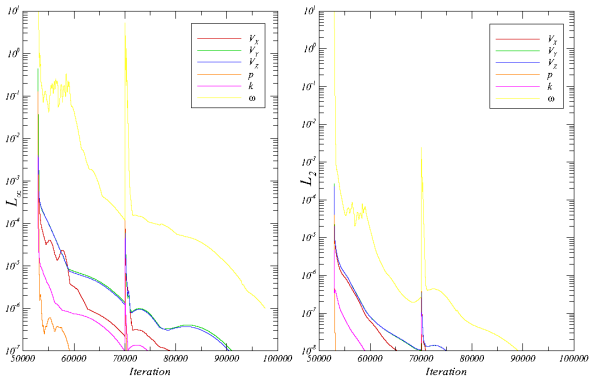

(a) Grid 21M, $k-\omega$ SST Model.

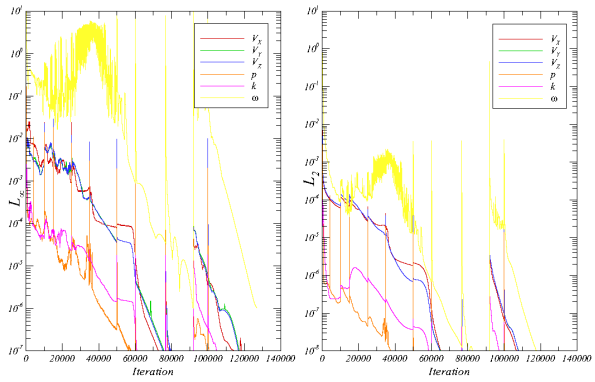

(b) Grid 38M, $k-\omega$ SST Model.

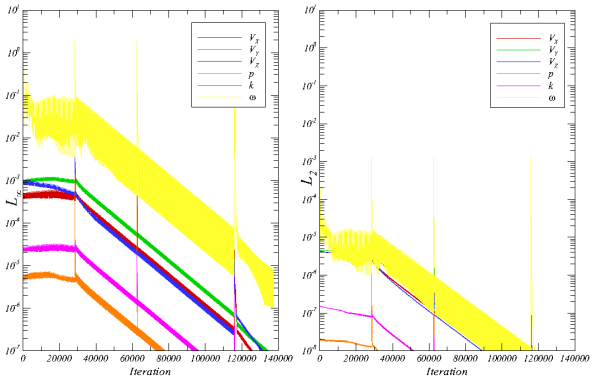

(c) Grid 38M, $k-\omega$ SST Model. $Re = 1.46 \times 10^6$.

Figure B.2: Residuals graphics for the grids 21M, 38M, and 38M with $Re = 1.46 \times 10^6$. $k-\omega$ SST Model.

B.2 $\gamma - \tilde{\mathrm{Re}}_{\theta_t}$ calculations

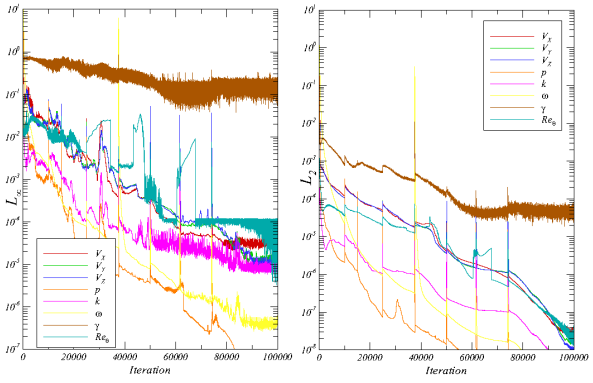

(a) Grid 38M, $\gamma - \tilde{Re}_{\theta_t}$ Model.

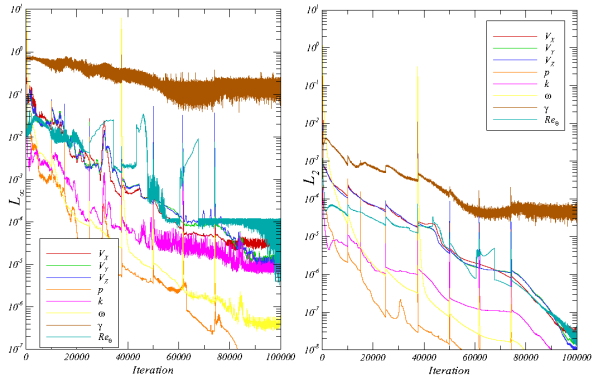

(b) Grid 38M, $\gamma - \tilde{Re}_{\theta_t}$ Model with $Re = 1.46 \times 10^6$.

Figure B.3: Residuals graphics for the grids 38M and 38M with $Re = 1.46 \times 10^6$. $\gamma - \tilde{Re}_{\theta_t}$ Model, with $Tu = 1.2\%$.

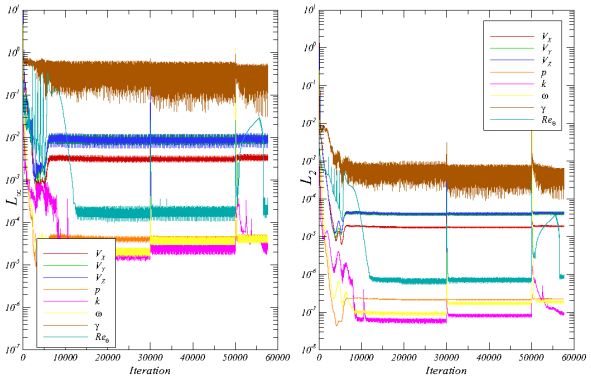

(a) Grid 1M, $\gamma - \tilde{Re}_{\theta_t}$ Model.

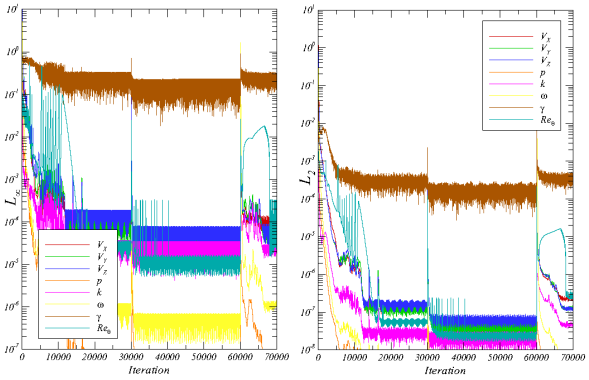

(b) Grid 2M, $\gamma - \tilde{Re}_{\theta_t}$ Model.

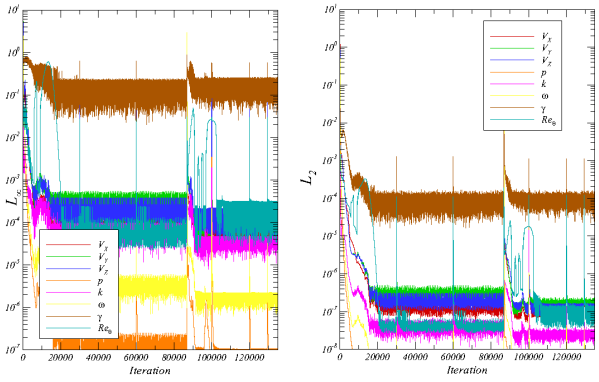

(c) Grid 6M, $\gamma - \tilde{Re}_{\theta_t}$ Model.

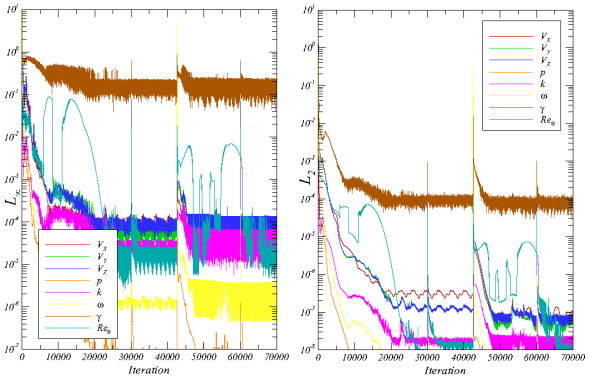

(d) Grid 10M, $\gamma - \tilde{Re}_{\theta_t}$ Model.

Figure B.4: Residuals graphics for the grids 1M, 2M, 6M, and 10M. $\gamma - \tilde{Re}_{\theta_t}$ Model, with $Tu = 1.5\%$.

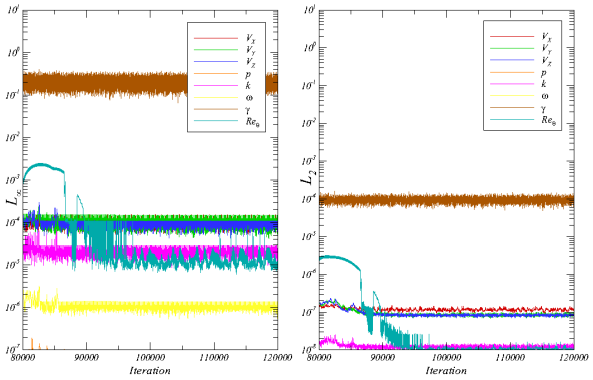

(a) Grid 21M, $\gamma - \tilde{Re}_{\theta_t}$ Model.

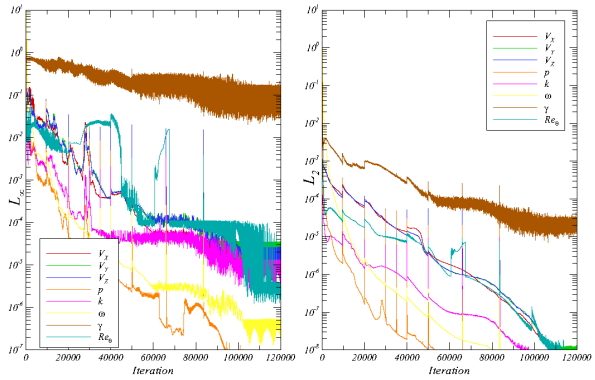

(b) Grid 38M, $\gamma - \tilde{Re}_{\theta_t}$ Model.

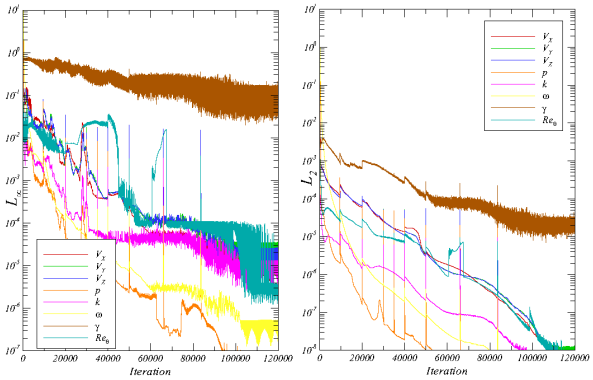

(c) Grid 38M, $\gamma - \tilde{Re}_{\theta_t}$ Model. $Re = 1.46 \times 10^6$.

Figure B.5: Residuals graphics for the grids 21M, 38M, and 38M with $Re = 1.46 \times 10^6$. $\gamma - \tilde{Re}_{\theta_t}$ Model, with $Tu = 1.5\%$.